Correction date: October 30, 2014 (Revision 2)

Temperature dependence of crystal structure of $CaGeO_3$ high-pressure perovskite phase and experimental determination of its Debye temperatures studied by low- and high-temperature single crystal X-ray diffraction

Akihiko Nakatsuka,[1,*] Shoichi Kuribayashi,[1] Noriaki Nakayama,[1] Hiroshi Fukui,[2] Hiroshi Arima,[3] Akira Yoneda,[4] and Akira Yoshiasa[5]

[1]Graduate School of Science and Engineering, Yamaguchi University, Ube 755-8611, Japan
[2]Graduate School of Material Science, University of Hyogo, Ako 678-1297, Japan
[3]Institute for Materials Research, Tohoku University, Sendai 980-8577, Japan
[4]Institute for Study of the Earth's Interior, Okayama University, Misasa 682-0193, Japan
[5]Graduate School of Science and Technology, Kumamoto University, Kumamoto 860-8555, Japan

* Corresponding author. Tel: +81-836-85-9651; Fax: +81-836-85-9201.
E-mail: tuka@yamaguchi-u.ac.jp

ABSTRACT

Single crystal X-ray diffraction study of $CaGeO_3$ perovskite has been conducted over the temperature range of 98 to 1048 K. The crystal begins to deteriorate at a temperature above about 900 K and completely amorphizes by 980 K. The diffraction-intensity distribution and the structure refinements indicate that the *Pbnm* structure is kept until the occurrence of amorphization. The obtained unit-cell parameters, unit-cell volumes, bond lengths and displacement parameters increase monotonously with increasing temperature. Thus, no evidence for the existence of the *Cmcm* high-temperature phase, previously suggested above 520 K, is observed. The Ge–O bond lengths show much smaller thermal expansions than the Ca–O bond lengths; the former ranges between $0.42(2) \times 10^{-5}$ K^{-1} and $0.57(2) \times 10^{-5}$ K^{-1}, and the latter between $1.58(4) \times 10^{-5}$ K^{-1} and $3.96(6) \times 10^{-5}$ K^{-1}. The Debye temperatures and static disorder components for each constituent atom were determined by applying the Debye model to the temperature dependence of mean square displacements (MSDs) of the atoms. Consequently, no significant static disorder components can be detected in each atom. The Debye temperatures averaged over all directions, obtained from the Debye model fitting to U_{eq}, yield the harmonic one particle potential coefficients of 4.76(2) eVÅ^{-2} for Ca, 11.0(1) eVÅ^{-2} for Ge, 5.02(2) eVÅ^{-2} for O1 and 5.33(5) eVÅ^{-2} for O2. These values become larger in order of Ca < O1 < O2 << Ge, which shows that the one particle potential of Ge is much narrower than that of Ca. This relationship between Ca and Ge is consistent reasonably with bonding stiffness expected from the thermal expansion coefficients of the bond lengths. The anisotropies of MSDs are remarkable in O1 and O2 atoms as a consequence of the strong interaction with adjacent Ge atoms, forming the rigid bonds with these O atoms.

In comparison of the three *Pbnm* orthorhombic perovskites of $CaGeO_3$, $CaTiO_3$ and $MgSiO_3$, all of these have the BO_6 octahedra more rigid than the AO_{12} polyhedra (A = Ca or Mg; B = Ge, Ti or Si) and the tilt angles of BO_6 octahedra are the largest in $MgSiO_3$ perovskite. These observations indicate that if $MgSiO_3$ perovskite under high pressures undergoes the same sequence of the high-temperature phase transitions as $CaTiO_3$ perovskite, the phase boundaries have positive Clapeyron slopes and the phase transition temperatures should become further much higher than those (1512 K for the *Pbnm* to *I4/mcm* transition and 1635 K for the *I4/mcm* to $Pm\bar{3}m$ transition) observed in $CaTiO_3$ perovskite at ambient pressure. This leads to the conclusion that the high-temperature phase transition to a perovskite phase with different symmetry under high pressures previously suggested in $MgSiO_3$ perovskite is unlikely.

Keywords: $CaGeO_3$, perovskite, single crystal X-ray diffraction, phase transition, thermal expansion, Debye temperature, one particle potential

INTRODUCTION

$MgSiO_3$ perovskite is the most dominant constituent in the Earth's lower mantle. Because of such importance, studies on physical properties and crystal structure of $MgSiO_3$ perovskite have extensively been performed form both sides of experiments (e.g., Horiuchi et al. 1987; Kudoh et al. 1987; Ross and Hazen 1989) and theoretical simulations (e.g. Dekura et al. 2013; Tsuchiya et al. 2004; Wentzcovitch et al. 2004). However, the quenched samples of $MgSiO_3$ perovskite recovered at ambient condition are well known to rapidly amorphize under electron beam in transmission electron microscope, and such low thermal stability has severely limited the experimental investigations of its structural and physical properties at high temperatures (Madon et al. 1989). Because of this, various analogues with higher thermal stability, such as $CaGeO_3$ (McMillan and Ross 1988; Durben et al. 1991; Liu et al. 1991), $CaTiO_3$ (McMillan and Ross 1988; Guyot et al. 1993; Liu and Liebermann 1993; Ali and Yashima 2005; Yashima and Ali 2009) and $NaMgF_3$ (Yoshiasa et al. 2005) have been investigated to help the understanding for high-temperature properties of $MgSiO_3$ perovskite.

In particular $CaGeO_3$ is an excellent analogue of $MgSiO_3$, because both compounds not only are of the $A^{2+}B^{4+}O_3$-type but also exhibit the similar sequence of phase transitions at high pressures and high temperatures of pyroxenoid (wollastonite) type → tetragonal garnet type → orthorhombic perovskite type (Prewitt and Sleight 1969; Susaki et al. 1985). The perovskite phase of $CaGeO_3$ was confirmed to have the *Pbnm* structure (orthorhombic), isostructural with $MgSiO_3$ perovskite, at ambient condition by single crystal X-ray diffraction (Sasaki et al. 1983), although it had previously been indexed as a cubic perovskite (Ringwood and Major 1967). The crystal structure consists of a network of corner-linked GeO_6 octahedra with the larger Ca atoms located at the centers of cavities in the network and is distorted largely from the ideal cubic structure with $Pm\bar{3}m$ symmetry owing to the tilting of GeO_6 octahedra (Figs. 1a–1c). Later, Liu et al. (1991) suggested from the high-temperature powder X-ray diffraction that $CaGeO_3$ perovskite undergoes the phase transition to the *Cmcm* structure (orthorhombic) near 520 K at ambient pressure. This suggestion was based on (1) the appearance of the reflections that should be forbidden in *Pbnm* but allowed in *Cmcm* and (2) the convergence of the *a*- and *b*-axis lengths above 520 K. However, in the observation (1), the very weak peaks assigned as the forbidden reflections in *Pbnm* seem to be invisible as far as we see the powder X-ray diffraction pattern shown by Liu et al. (1991). In the observation (2), the determination of the unit-cell parameters from their Rietveld refinements was performed by fixing the atomic positions of O atoms to the values given by the single-crystal structure refinement at room temperature (Sasaki et al. 1983). No heat capacity anomaly at 520 K was also detected in their calorimetric measurements (Liu et al. 1991), which is consistent with the implications of the high-temperature Raman scattering study (Durben et al. 1991) that no symmetry breaking transition occurs in $CaGeO_3$ perovskite at high temperatures. There is thus some doubt as for the existence of the *Cmcm* high-temperature phase, and the sufficient structural knowledge at high temperatures has not been provided even in the *Pbnm* phase.

We here report the single crystal X-ray diffraction study of $CaGeO_3$ perovskite in the range of 98 to 1048 K, to investigate its structural behavior at high temperatures. Together with the examination as for whether or not the phase transition to the *Cmcm* phase is present, temperature dependence of the crystal structure of the *Pbnm* phase is discussed with attention to thermal expansions and tilting of GeO_6 octahedra. Moreover, the harmonic one particle potentials of each atom are evaluated from the Debye temperatures determined from temperature dependence of mean square displacements (MSDs) of atoms to gain knowledge of bonding stiffness.

EXPERIMENTS AND ANALYSIS

Single-crystal growth under high pressure

Single crystals of $CaGeO_3$ perovskite were grown at 12 GPa and 1253 K using a Kawai-type high-pressure apparatus installed at the ISEI of Okayama University. A 14 mm regular octahedron of a sintered MgO containing 5% of Cr_2O_3 was employed as a pressure-transmitting-medium. The starting material was powdered $CaGeO_3$ wollastonite prepared by solid-state reaction of special grade reagents of $CaCO_3$ and GeO_2, and was mixed with a 5 mol% of PbO flux. The mixture was enclosed in a gold capsule and then set in the center of a MgO sleeve by inserting ZrO_2 plugs into the upper- and lower-ends of the sleeve. After that, the MgO sleeve was inserted into a cylindrical graphite heater and then put into a ZrO_2 sleeve embedded in the MgO octahedron; the ZrO_2 sleeve was used as a thermal insulator. This cell assembly was set in the anvil assembly of tungsten carbide cubes with truncated edge lengths of 7 mm, and then was compressed with the aid of the high pressure apparatus. The sample temperature was monitored by the W25%Re-W3%Re thermocouple with 0.05 mm in diameter. The junction of the thermocouple was put at the midpoint of the outer surface of the MgO sleeve. No correction was made for the pressure effect on emf. After being kept under a desired condition (12 GPa, 1253 K) for 1 hour, the product was quenched by shutting off the electric power supply. The pressure was released slowly and the product was recovered at ambient condition. Numerical single crystals of $CaGeO_3$ perovskite with the size of about 100–200 μm were found in the recovered sample.

X-ray diffraction intensity measurements and structure refinements

The single crystal with the size of $0.15 \times 0.14 \times 0.14$ mm^3 was selected and put into a silica-glass capillary for X-ray diffraction experiments. The experiments were conducted in the range of 98 to 1048 K using a Rigaku AFC-7R four-circle diffractometer with a graphite-monochromatized Mo Kα radiation (λ = 0.71069 Å) at the operating condition of 60 kV and 250 mA. The experiments below room temperature were conducted by directly cooling the crystal through a continuous cold N_2 gas flow generated using a Rigaku GN2 low temperature apparatus. In the experiments above room temperature, high temperature was achieved by a continuous flow of N_2 gas heated by electric resistance heater and thereby the crystal was directly heated. Prior to the data collections, sample temperatures were calibrated using a K-type thermocouple set exactly at the sample position. Temperature fluctuation during the data collections was kept within ±0.2 K. The unit-cell parameters at 33 temperature-points in the range of 98 to 898 K were determined by the least-squares method from a set of 25 reflections within the range of $46° \leq 2\theta \leq 50°$. X-ray diffraction intensity data within $2° \leq 2\theta \leq 100°$ were collected at 18 temperature-points in this temperature range using the continuous ω–2θ scan mode. Between 2446 and 2522 reflections were measured for each temperature. The intensity data were corrected for Lorentz-polarization factors and absorption effects (ψ-scan method). After these corrections, the intensity data were averaged in Laue symmetry *mmm* to give between 1123 and 1156 independent reflections for each temperature. Of these, independent reflections with $F_o \leq 3\sigma(F_o)$ were eliminated. Even if independent reflections had intensities of $F_o > 3\sigma(F_o)$ after averaging, those averaged from data set of equivalent reflections including reflection(s) with $F_o \leq 3\sigma(F_o)$ were also discarded since these reflections were potentially affected by multiple scattering. Moreover, independent reflections with $(\sin\theta)/\lambda < 0.329$ Å^{-1} were eliminated to reduce secondary extinction effects and to avoid dependence on atomic charge as far as possible in the choice of atomic scattering factors. Finally, between 653 and 844 independent reflections were used in the present refinements at each temperature. Internal residuals of the equivalent reflections (R_{int}) varied between 0.0092 and 0.0203 for each temperature.

The structure refinements were carried out by minimizing the function $\sum w(F_o - F_c)^2$ using a full matrix least-squares program RADY (Sasaki 1987). Scattering factors of Ca^{2+}, Ge^{4+} (*International Tables for Crystallography*, Table 6.1.1.3; Wilson 1992) and O^{2-} (Tokonami 1965) were used. Anomalous dispersion coefficients for each scattering factor were taken from *International Tables for Crystallography* (Table 4.2.6.8; Wilson 1992). Several correction models for the secondary extinction effects were attempted during the refinements, and the isotropic correction of Type I (Becker and Coppens 1974a, 1974b) with a Lorentzian mosaic spread distribution model yielded the best fits. The structure refinements at each temperature converged smoothly to R = 0.0142–0.0229 and wR = 0.0117–0.0184. The summary of data collection and refinement parameters is given in Table 1. The positional parameters and equivalent isotropic displacement parameters (U_{eq}) are given in Table 2. CIF is available on deposit.

RESULTS AND DISCUSSION

Evidence for absence of the phase transition to the *Cmcm* structure

As shown in Figure 1c, the *Pbnm* orthorhombic and *Cmcm* orthorhombic structures have the approximate unit-cell dimensions of $\sqrt{2} \times \sqrt{2} \times 2$ and $2 \times 2 \times 2$ to the pseudo-cubic lattice, respectively. The relationship among their unit-cell edge lengths is expressed as $a_p \approx \sqrt{2}a_c/2 \approx \sqrt{2}a_0$, $b_p \approx \sqrt{2}b_c/2 \approx \sqrt{2}a_0$ and $c_p \approx c_c \approx 2a_0$, where the subscripts "p", "c" and "0" represent *Pbnm*, *Cmcm* and pseudo-cubic structures, respectively. The temperature dependence of the present unit-cell parameters (a_p, b_p, c_p, α_p, β_p, γ_p) and volume (V_p) measured by assuming the $\sqrt{2} \times \sqrt{2} \times 2$ lattice is shown in Figures 2 and 3, respectively. The a_p, b_p, c_p and V_p increase monotonously with increasing temperature. The a_p approaches to b_p while keeping $a_p < b_p$ up to about 680 K, and then a_p gets ahead of b_p above this temperature after both agreed (Fig. 2a). During such variations of the unit-cell edge lengths, the α_p, β_p and γ_p angles are independent of temperature and exhibit no deviation from 90° (Fig. 2b). This situation continues up to about 900 K, but the diffraction peaks begin to broaden above this temperature and completely disappear by 980 K (Fig. 4). This agrees well with the Raman scattering study by Durben et al. (1991), which reported that $CaGeO_3$ perovskite, metastable at ambient pressure, amorphizes near 923 K. They also reported that the amorphous phase is an intermediate phase and recrystallizes to the thermodynamically stable wollastonite phase near 1023 K. However, no diffraction peak could be detected in our single crystal X-ray diffraction experiments up to 1048 K after the amorphization. This is probably because the present sample recrystallized as a fine-grained polycrystalline assemblage.

The *Cmcm* structure requires the $2 \times 2 \times 2$ lattice to be orthorhombic. This shows that if the phase transition of *Pbnm* to *Cmcm* occurs, the unit-cell parameters measured assuming the $\sqrt{2} \times \sqrt{2} \times 2$ lattice must satisfy the condition of "$a_\mathrm{p} = b_\mathrm{p}$ and $\gamma_\mathrm{p} \neq 90^\circ$" at the phase transition point and above, as illustrated in Figure 5. The symmetry constraints also require that this phase transition must necessarily be first order (Durben et al. 1991; Liu et al. 1991). However, the present data shows that the condition of "$a_\mathrm{p} = b_\mathrm{p}$ and $\gamma_\mathrm{p} \neq 90^\circ$" is not satisfied over the investigated temperature range and no resolvable discontinuity is observed in the temperature dependence of the unit-cell edge lengths and volume (Figs. 2 and 3).

To gain further evidence for the absence of the *Cmcm* high-temperature phase, we measured ω-scan profiles at positions of reflections that should be forbidden in the *Pbnm* structure but allowed in the *Cmcm* structure, at the 9 temperature-points in the range between 98 and 898 K. As examples, the profiles measured at the positions of 104, 300 and 302 reflections in the $\sqrt{2} \times \sqrt{2} \times 2$ lattice (corresponding to 114, 330 and 332 reflections in the $2 \times 2 \times 2$ lattice, respectively) are shown in Figure 6. As shown in this figure, none of these reflections could be detected at all over the investigated temperature range. The coincidence of equivalent-reflection intensities assuming the *Pbnm* structure is much better than that assuming the *Cmcm* structure over the investigated temperature range (e.g., $R_\mathrm{int} = 0.0125$ for *Pbnm* and $R_\mathrm{int} = 0.0495$ for *Cmcm* at 723 K). Indeed, the crystal structures were successfully refined in the *Pbnm* structure over the investigated temperature range, and the reliability indices reached $R = 0.0142$–0.0229 and $wR = 0.0117$–0.0184 for each temperature. Meanwhile, the refinements assuming *Cmcm* resulted in much higher reliability indices (e.g., $R = 0.0836$ and $wR = 0.0487$ at 723 K) with non-positive-definite anisotropic displacement parameters. It is evident from these observations that the phase transition of *Pbnm* to *Cmcm*, suggested by Liu et al. (1991), is absent and that the crystal structure keeps *Pbnm* orthorhombic symmetry over the investigated temperature range although the temperature dependence of a_p and b_p intersects at about 680 K. This conclusion agrees with the high-temperature Raman scattering study (Durben et al. 1991) that showed no evidence for the phase transition in $CaGeO_3$ perovskite.

The high-temperature powder X-ray diffraction study of Liu et al. (1991) reported that a_p and b_p

converge at about 520 K. This convergence is a base of their argument that the phase transition of *Pbnm* to *Cmcm* occurs at this temperature. However, in the present data, such convergence is not observed at this temperature (Fig. 2a). To examine the reason for this discrepancy, we show in Figure 7 the temperature dependence of $\sqrt{2}a_p/2$, $\sqrt{2}b_p/2$ and $c_p/2$, corresponding to the unit-cell edge lengths in the pseudo-cubic lattice. These lengths are very close (e.g. $\sqrt{2}a_p/2$ = 3.7299(3) Å, $\sqrt{2}b_p/2$ = 3.7323(4) Å, $c_p/2$ = 3.7323(3) Å at 523 K). In particular, it is noteworthy that the temperature dependence of the present $\sqrt{2}b_p/2$ and $c_p/2$ (Fig. 7) intersects at about 520 K, the same temperature as the convergence point of a_p and b_p suggested by Liu et al. (1991). Such similarity of the unit-cell edge lengths makes it difficult to index the powder X-ray diffraction pattern especially around this temperature. The discrepancy in temperature dependence of a_p and b_p between our and Liu's studies is thus likely to originate in mis-indexing of powder X-ray diffraction pattern by the latter study.

Thermal expansion

Unit-cell volume. The unit-cell volume data (Fig. 3) were fitted to the following equation (Suzuki et al. 1979) derived from the Grüneisen theory of volumetric thermal expansion, using a non-linear weighted least-squares method:

$$V(T) = \frac{V_t}{2k_0 a_v}\left(1 + 2k_0 - \sqrt{1 - \frac{4k_0 U(T)}{Q_0}}\right) \quad \cdots\cdots (1)$$

$$U(T) = 9nRT\left(\frac{T}{\Theta_D}\right)^3 \int_0^{\frac{\Theta_D}{T}} \frac{x^3}{\exp(x) - 1} dx \quad \cdots\cdots (2)$$

where $Q_0 = K_0V_0/\gamma_G$, $k_0 = (dK_0/dP - 1)/2$ and $a_v = V_t/V_0$; V_0 and K_0 are the volume and the bulk modulus at 0 K, respectively, and V_t is the volume at a reference temperature t; γ_G is the Grüneisen parameter, $U(T)$ the internal energy, n the number of atoms in the formula unit, R the gas constant, Θ_D the Debye temperature and T the absolute temperature. The fitting parameters resulted in Θ_D = 666(16) K, Q_0 = 3.92(2) × 10^6 J/mol and a_v (= V_{298}/V_0) = 1.00397(7) by fixing k_0 to 2.7. This fixed k_0 value was approximated by substituting the pressure derivative of isothermal bulk modulus $\partial K_T/\partial P$ (= 6.4) at 300 K (Liu and Li 2007; Liu et al. 2008) for dK_0/dP.

Liu et al. (2008) approximated the temperature dependence of isothermal bulk modulus K_T of $CaGeO_3$ perovskite in the temperature range of their experiments (300 ≤ T ≤ 1100 K) by the following linear equation:

$$K_T(T) = K_T(300\text{ K}) + (\partial K_T/\partial T)_P(T - 300\text{ K})$$
$$= 193 - 0.025(T - 300)\text{ GPa} \quad \cdots\cdots (3)$$

Alternatively, its temperature dependence might be represented by the following theoretical equation that was originally derived for the adiabatic bulk modulus $K_S(T)$ (Anderson 1966):

$$K_T(T) = K_0 - (g/V_0)U(T) \quad \cdots\cdots (4)$$

where $g = \gamma_G\delta$; δ is the Anderson-Grüneisen parameter. To evaluate the K_0 value, the data within the temperature range of Liu's experiments ($300 \le T \le 1100$ K) calculated from Equation (3) were fitted to Equation (4). The fit converged to K_0 = 196 GPa and g = 6.57 by fixing at Θ_D = 666 K obtained above, yielding γ_G (= K_0V_0/Q_0) = 1.55 and hence δ (= g/γ_G) = 4.24. This γ_G is in fair agreement with the value (1.35) from the high-pressure experiments (Liu and Li 2007; Liu et al. 2008).

The temperature dependence of the volumetric thermal expansion coefficients $\alpha_V(T)[= 1/V(T) \cdot dV(T)/dT]$ obtained by differentiation of Equation (1) is also given in Figure 3. The $\alpha_V(T)$ increases steeply with heating up to about 350 K, after which it increases almost linearly with a gentle slope above about 650 K.

Unit-cell edge lengths and bond lengths. Figures 8 and 9 show the temperature dependence of the bond lengths and their thermal expansion coefficients $\alpha_L(T)[= 1/L(T) \cdot dL(T)/dT]$ together with those of the unit-cell edge lengths, respectively, where $L(T)$ is geometric dimensions such as unit-cell edge lengths and bond lengths as a function of temperature and functions obtained from the parabolic fits were employed for $L(T)$. The resulting $\alpha_L(T)$ data was fitted to the approximation $\alpha_L(T) = \varepsilon_0 + \varepsilon_1 T + \varepsilon_2 T^{-2}$ ($\varepsilon_2 \le 0$) (Fei 1995), and the coefficients ε_0, ε_1 and ε_2 determined for each geometric observation are tabulated in Table 3. For comparison with other compounds, the conventional mean thermal expansion coefficients $\langle\alpha_L\rangle$, determined from the fits to the linear equation $L(T) = L_r\{1 + \langle\alpha_L\rangle(T - T_r)\}$, are also listed in Table 3, where L_r is geometric dimensions at a reference temperature T_r, and 298 K was adopted as T_r in the present study.

The thermal expansivities of the unit-cell edges increase in order of $b_p < c_p < a_p$. Such anisotropy in the thermal expansion is consistent with those of other *Pbnm* perovskites such as $CaTiO_3$ (Liu and Liebermann 1993) and $MgSiO_3$ (Ross and Hazen 1989). In ABO_3 perovskites with the *Pbnm* structure, the great structural distortion due to the titling of BO_6 octahedra yields much longer separations between an A atom and four of twelve O atoms surrounding its A atom. In $CaGeO_3$ perovskite, the four longer Ca···O separations [Ca···O1^{i}, Ca···O1^{ii}, Ca···O2^{iii} and Ca···O2^{iv}] range between 2.856(2) and 3.072(1) Å at 298 K, and the remaining eight shorter ones [Ca···O1^{v}, Ca···O1, Ca···O2^{vi}, Ca···O2^{v}, Ca···O2^{vii}, Ca···O2^{viii}, Ca···O2^{ix} and Ca···O2^{x}] range between 2.343(2) and 2.599(1) Å at 298 K (Table 4). The bond valence sums assuming the twelve-fold coordinated Ca atom deviate largely from the valences of Ca and O atoms, whereas those assuming the eight-fold coordinated Ca atom agree well with their valences (Table 4). Thus, the four longer Ca···O separations are not involved in chemical bonding. This can also be understood from the observations that these separations exhibit largely negative thermal expansions (Fig. 9 and Table 3).

The symmetrically non-equivalent three Ge–O bond lengths are very close as shown in Fig. 8 and Table 4. They do not depend largely on temperature and have much smaller thermal expansion coefficients than Ca–O bond lengths; the former ranges between 0.42(2) × 10^{-5} K^{-1} and 0.57(2) × 10^{-5} K^{-1} and the latter varies between 1.58(4) × 10^{-5} K^{-1} and 3.96(6) × 10^{-5} K^{-1} (Table 3). The symmetrical constraints always request 180° for O1–Ge–O1^{xi}, O2^{vii}–Ge–O2^{xiii} and O2^{ix}–Ge–O2^{xii} angles, and the remaining twelve O–Ge–O angles in a GeO_6 octahedron vary between 89.22(1)° and 90.78(1)° at 98 K. These variable bond-angles only show the fluctuation of 0.3° at maximum in the investigated temperature range and hardly depend on temperature. Thus, individual GeO_6 is rigid and keeps a nearly regular octahedron independent of temperature. This shows that the response of $CaGeO_3$ perovskite structure to temperature is dominated mainly by the tilting between corner-linked GeO_6 octahedra as will be described in the next section.

Temperature dependence of GeO_6 octahedral tilting

The octahedral tilting can be characterized by the three tilt angles (Glazer 1972, 1975). We here use ϕ_i^+, ϕ_i^- and ϕ_i^0 ($i = x, y$ or z) after Yashima and Ali (2009) as a notation of the tilt angles. The ϕ_i^+, ϕ_i^- and ϕ_i^0 indicate the in-phase tilt angle of octahedra, the out-of-phase tilt angle and no octahedral tilting about i-axis ($i = x, y$ or z), respectively. The x-, y- and z-axes represent $[100]_0$, $[010]_0$ and $[001]_0$, respectively, where the subscript "0" represents the pseudo-cubic lattice. The tilting system of *Pbnm* orthorhombic perovskites is described by two identical out-of-phase tilting about the $[100]_0$ and $[010]_0$ axes ($\phi_x^- = \phi_y^-$) and an in-phase tilting about the $[001]_0$ axis (ϕ_z^+), being expressed as $\phi_x^-\phi_y^-\phi_z^+$ ($\phi_x^- = \phi_y^-$). This tilting system is also described as $a^-a^-c^+$ using well-known Glazer's notation (Glazer 1972, 1975). The tilt angles have often been defined only from the fractional coordinates of O atoms as in Kennedy et al. (1999). However, the tilt angles calculated in this way will more or less be influenced by the variation of distortion of octahedra themselves with temperature. We here calculated them via the symmetry-adapted mode approach, which can completely separate the tilts and distortions of octahedra. In terms of this approach, the tilt angle ϕ is given by $\phi = \tan^{-1}(2d')$ (Wang and Angel 2011), where d' is the amplitude of octahedral tilt mode. The d' values are converted from the standard supercell-normalized amplitude "*As*" and "*normfactor*" calculated using the program *ISODISTORT* (or the earlier *ISODISPLACE*; Campbell et al. 2006). The details are described in Wang and Angel (2011).

Figure 10 shows the temperature dependence of the tilt angles ϕ_x^- (= ϕ_y^-) and ϕ_z^+ of GeO_6 octahedra in $CaGeO_3$ perovskite calculated in this way, together with that of the positional parameters *x* and *y* of Ca atoms, located at the coordinates (*x*, *y*, 0.25). For comparison, that of $CaTiO_3$ perovskite (Yashima and Ali 2009) with the same $A^{2+}B^{4+}O_3$-type *Pbnm* structure as $CaGeO_3$ perovskite is also shown in this figure. The ϕ_x^- and ϕ_z^+ in $CaGeO_3$ perovskite decrease with increasing temperature (Fig. 10a). The Ca atom approaches its ideal position (0, 0, 0.25), corresponding to the Ca position in the $Pm\bar{3}m$ cubic structure, with increasing temperature (Fig. 10b). These tendencies are consistent with the case of $CaTiO_3$ perovskite. The negative thermal expansions of the four non-bonding Ca···O separations (Fig. 9 and Table 3) are a consequence of such decrease in structural distortion and a sign of the approach to the $Pm\bar{3}m$ cubic structure with twelve equivalent Ca–O bond lengths and without any octahedral tilting ($\phi_x^0\phi_y^0\phi_z^0$).

The existence of the intermediate orthorhombic phase *Cmcm* at high temperatures had previously been suggested in $CaTiO_3$ perovskite (Guyot et al. 1993; Kennedy et al. 1999) as well. However, the recent high-temperature powder neutron diffraction studies of $CaTiO_3$ perovskite (Ali and Yashima 2005; Yashima and Ali 2009) proved the absence of *Cmcm* phase, as well as in the present $CaGeO_3$ perovskite, and instead reported the phase transitions of orthorhombic *Pbnm* → tetragonal *I4/mcm* at 1512 K and tetragonal *I4/mcm* → cubic $Pm\bar{3}m$ at 1635 K. Unfortunately, the present sample of metastable $CaGeO_3$ perovskite, recovered at ambient condition, amorphized at the temperature beyond 900 K. However, $CaGeO_3$ perovskite may undergo the same sequence of the high-temperature phase transitions as $CaTiO_3$ perovskite under high pressures, from the similarity in the temperature dependence of crystal structure between both compounds described above.

Temperature dependence of MSDs of atoms

Figures 11 and 12 show the temperature dependence of equivalent isotropic displacement parameter U_{eq} and MSD_{hkl} of each atom, respectively, where U_{eq} corresponds to mean square displacement (MSD) of atom averaged over all directions; MSD_{hkl} is MSD of atom in the $[hkl]_\mathrm{p}$ direction and the subscript "p" represents the *Pbnm* orthorhombic lattice. The MSD determined by diffraction method includes the contributions of both static and dynamic disorders, and can be described on the basis of the Debye model as follows (Willis and Pryor 1975):

$$\mathrm{MSD} = \langle u^2\rangle_\mathrm{s} + \langle u^2\rangle_\mathrm{d} = \langle u^2\rangle_\mathrm{s} + \frac{3\hbar^2 T}{mk_\mathrm{B}\Theta_\mathrm{D}^2}\left[\frac{T}{\Theta_\mathrm{D}}\int_0^{\frac{\Theta_\mathrm{D}}{T}}\frac{x}{\exp(x)-1}dx + \frac{\Theta_\mathrm{D}}{4T}\right] \quad \cdots\cdots (5)$$

where $\langle u^2\rangle_\mathrm{s}$ is the temperature-independent static disorder component, $\langle u^2\rangle_\mathrm{d}$ the temperature-dependent dynamic disorder component, m the mass of atoms, k_B the Boltzmann constant, $\hbar$ the reduced Planck constant, Θ_D the Debye temperature and T the absolute temperature. A non-linear least squares fitting of the U_eq or MSD_{hkl} data to Equation (5) (Debye model fitting) allows us to evaluate $\langle u_\mathrm{eq}{}^2\rangle_\mathrm{s}$ and $\Theta_{\mathrm{D}_\mathrm{eq}}$, or, $\langle u_{hkl}{}^2\rangle_\mathrm{s}$ and $\Theta_{\mathrm{D}_{hkl}}$, where $\langle u_\mathrm{eq}{}^2\rangle_\mathrm{s}$ and $\Theta_{\mathrm{D}_\mathrm{eq}}$, determined from the U_eq data, are the static disorder component and the Debye temperature averaged over all directions, respectively; $\langle u_{hkl}{}^2\rangle_\mathrm{s}$ and $\Theta_{\mathrm{D}_{hkl}}$, determined from the MSD_{hkl} data, are the static disorder component and the Debye temperature in the $[hkl]_\mathrm{p}$ direction, respectively.

The temperature dependence of U_eq and MSD_{hkl} for each atom is well represented by the Debye model over the investigated temperature range (Figs.11 and 12). Their variations are approximately linear in the high-temperature range and begin to flatten below about 200~300 K. This behavior at low temperatures is an obvious indication of the zero-point energy contribution. The $\langle u_\mathrm{eq}{}^2\rangle_\mathrm{s}$ values resulted in –0.0003(1) Å^2 for Ca, –0.0004(1) Å^2 for Ge, 0.0000(1) Å^2 for O1 and –0.0007(2) Å^2 for O2, and can be regarded as zero within the error of about 3σ although some of them converged to the slightly negative values. Therefore, we can consider that the static disorder is not present in each atom, and the Debye model fitting was finally performed by fixing at $\langle u_\mathrm{eq}{}^2\rangle_\mathrm{s} = 0$ or $\langle u_{hkl}{}^2\rangle_\mathrm{s} = 0$. The final values of $\Theta_{\mathrm{D}_\mathrm{eq}}$ and $\Theta_{\mathrm{D}_{hkl}}$ obtained in this way are provided in Table 5. The average of the resulting $\Theta_{\mathrm{D}_\mathrm{eq}}$ values for each atom [= $\{\Theta_{\mathrm{D}_\mathrm{eq}}(\mathrm{Ca}) + \Theta_{\mathrm{D}_\mathrm{eq}}(\mathrm{Ge}) + \Theta_{\mathrm{D}_\mathrm{eq}}(\mathrm{O1}) + 2\Theta_{\mathrm{D}_\mathrm{eq}}(\mathrm{O2})\}/5$] is 636(2) K, being in agreement with the Debye temperature Θ_D of 666(16) K determined from the volumetric thermal expansion.

At high temperatures of $T > \Theta_\mathrm{D}$, where the contribution of zero-point energy is negligible, the dynamic disorder component, i.e. thermal vibration component, in Equation (5) reduces to $\langle u^2\rangle_\mathrm{d} = \{3\hbar^2/(mk_\mathrm{B}\Theta_\mathrm{D}^2)\}T$. The slope [$= 3\hbar^2/(mk_\mathrm{B}\Theta_\mathrm{D}^2)$] in this linear equation is equal to k_B/q when we assume the harmonic one particle potential $V_\mathrm{OPP}(u) = (q/2)\langle u^2\rangle_\mathrm{d}$ (Willis and Pryor

1975), where q is the one particle potential (OPP) coefficient. Therefore, the OPP coefficient q is related to the Debye temperature Θ_D by

$$q = \frac{mk_B^2\Theta_D^2}{3\hbar^2} \quad \cdots\cdots (6)$$

The increment of q value, corresponding to a force constant, indicates the enhancement of bonding stiffness. The substitution of $\Theta_{D_{eq}}$ for Θ_D in Equation (6) can provide the OPP coefficient, q_{eq}, averaged over all directions. The present q_{eq} values are calculated as 4.76(2) eVÅ^{-2} for Ca, 11.0(1) eVÅ^{-2} for Ge, 5.02(2) eVÅ^{-2} for O1 and 5.33(5) eVÅ^{-2} for O2, and become larger in order of Ca < O1 < O2 << Ge. This relationship between Ca and Ge is reasonably consistent with bonding stiffness expected from the thermal expansion coefficients of the bond lengths (Fig. 9 and Table 3). The q_{eq} values of O1 and O2 atoms are significantly smaller than those of O atoms observed usually in silicates (≈ 6 eVÅ^{-2}). For comparison with silicates, as an example, we show the q_{eq} values calculated using the $\Theta_{D_{eq}}$ data of pyrope ($Mg_3Al_2Si_3O_{12}$), a silicate garnet, reported by our previous study (Nakatsuka et al. 2011): 3.34(2) eVÅ^{-2} for ^{VIII}Mg, 8.36(4) eVÅ^{-2} for ^{VI}Al, 9.45(7) eVÅ^{-2} for ^{IV}Si, 5.89(2) eVÅ^{-2} for O, where the superscripts IV, VI and VIII represent the four-, six- and eight-fold coordination, respectively. It is noteworthy that the q_{eq} value of ^{VI}Ge in $CaGeO_3$ perovskite is significantly larger than that of ^{IV}Si in pyrope although the former atom has the higher coordination number and the longer distances to ligands than the latter atom. This large stiffness of ^{VI}Ge–O bonds can also be understood from the above observation that the distortion of GeO_6 octahedron is almost temperature-independent.

As shown in example at 298 K (Fig. 13), the atomic thermal vibration is almost isotropic in Ge atom over the investigated temperature range, but shows obvious anisotropies in Ca, O1 and O2 atoms. Such anisotropies are remarkable especially in O1 and O2 atoms, and their displacement ellipsoids elongate near perpendicularly to Ge–O1 and Ge–O2 bonds, respectively. When we focus on the O2–Ge–O2 linkage formed by an O2 atom and its adjacent O2 atom in a GeO_6 octahedron (such as O2^{vii}–Ge–O2^{xii}, O2^{xii}–Ge–O2^{xiii}, O2^{ix}–Ge–O2^{xiii} or O2^{vii}–Ge–O2^{ix} linkage in Fig. 13), the largest ellipsoid-axes of the corresponding two O2 atoms run out of the plane made by this O2–Ge–O2 linkage. The largest ellipsoid-axes of an O1 atom and its adjacent O2 atom in a GeO_6 octahedron are also under the similar situation. Such out-of-plane bending vibrations of Ge–O bonds correspond to the twisting vibrations of perovskite framework centered on Ge atoms, often discussed in spectroscopic studies of perovskite compounds. The displacement ellipsoids of O2 atoms elongate also toward Ca atoms, which is indicative of the stretching vibrations of Ca–O2 bonds. The same vibrational manners as these are observed over the investigated temperature range.

Meanwhile, the shortest ellipsoid-axes of O atoms run completely along $[001]_p$ for O1 and nearly along $[110]_p$ for O2 over the investigated temperature range. These directions are consistent nearly with the directions of Ge–O1 and Ge–O2 bonds, respectively (Fig. 13). Thus, the large anisotropies of MSDs of O1 and O2 atoms will originate in the strong interaction with adjacent Ge atoms, forming the rigid bonds with these O atoms. For a closer estimation of the bonding stiffness, we here evaluate the anisotropic OPP coefficients q_{hkl} by the substitution of $\Theta_{D_{hkl}}$ for Θ_D in Equation (6), where q_{hkl} is the OPP coefficient in the $[hkl]_p$ direction. The OPP coefficients of Ge and O1 atoms in the direction of Ge–O1 bond can be approximated by q_{001}(Ge) = 9.90(10) eVÅ^{-2} evaluated from $\Theta_{D_{001}}$(Ge) and q_{001}(O1) = 10.3(2) eVÅ^{-2} evaluated from $\Theta_{D_{001}}$(O1), respectively. Both values are comparable. The OPP coefficient of O2 atom in the direction of Ge–O2 bond can be approximated by q_{110}(O2) = 12.5(3) eVÅ^{-2} evaluated from $\Theta_{D_{110}}$(O2). These q_{hkl} values show that Ge–O2 bond is more rigid than Ge–O1 bond, as also expected from the thermal expansivities of both bonds (Fig. 9 and Table 3).

IMPLICATIONS

The present study has revealed that GeO_6 octahedra in $CaGeO_3$ perovskite are considerably rigid. Such knowledge of rigidities of polyhedra in perovskites is quite important because the relative compressibility of AO_{12} and BO_6 polyhedra in ABO_3 perovskites is closely associated with their phase transition behaviors under high pressures and high temperatures (Zhao et al. 2004; Angel et al. 2005). The compressibility ratio (β_B/β_A) of the two polyhedra is given by $\beta_B/\beta_A = M_A/M_B$ (Zhao et al. 2004), where the subscripts "A" and "B" represent the AO_{12} and BO_6 polyhedra, respectively. The parameter M_i (i = A or B) is usually defined as

$$M_i = (R_i N_i/B)\exp[(R_0 - R_i)/B] \quad \cdots\cdots (7)$$

where N_i and R_i are the coordination number of cations and the average bond length at ambient condition, respectively; R_0 and B the bond valence parameters. In most *Pbnm* orthorhombic perovskites, Equation (7) is a good approximation for M_B, but it is invalid for M_A because of considerable distortions of the AO_{12} polyhedra and the following approximation was proposed for its calculation (Zhao et al. 2004):

$$M_A = (8\,R_{A8}/B)\exp[(R_0 - R_{A8})/B] + (4\,R_{A4}/B)\exp[(R_0 - R_{A4})/B] \quad \cdots\cdots (8)$$

where R_{A8} and R_{A4} are the average distances of eight shorter A–O bonds and of four longer A–O separations, respectively. According to Angel et al. (2005), when the BO_6 octahedra are more rigid than the AO_{12} polyhedra (i.e., $M_A/M_B < 1$), the phase transition temperature T_c rises with increasing pressure as a consequence of the increase in the octahedral tilting; thus, the phase boundary has a positive Clapeyron slope ($dP/dT_c > 0$). Conversely, when the BO_6 octahedra are less rigid than the AO_{12} polyhedra (i.e., $M_A/M_B > 1$), T_c reduces with increasing pressure as a consequence of the decrease in the tilting; thus, the phase boundary has a negative Clapeyron slope ($dP/dT_c < 0$). When we here consider the three *Pbnm* orthorhombic perovskites of $CaGeO_3$ (the present study), $CaTiO_3$ (Yashima and Ali 2009) and $MgSiO_3$ (Sugahara et al. 2006), the M_A/M_B ratios at ambient condition calculated using Equation (7) for M_B and Equation (8) for M_A are 0.66, 0.56 and 0.67, respectively, where the bond valence parameters R_0 and B used here are the values quoted for the bond valence sum calculations in Table 4. It follows therefore that if these three perovskites undergo phase transitions to perovskite phases with different symmetries under high pressures and high temperatures, their phase boundaries have positive Clapeyron slopes. This result is quite significant for the understanding of phase transitions in the Earth's interior, especially in $MgSiO_3$ perovskite, the most dominant constituent in the Earth's lower mantle.

$MgSiO_3$ perovskite is now believed to undergo the phase transition to post-perovskite structure with $CaIrO_3$ structure, associated with the D" seismic discontinuity, at 125 GPa and 2500 K (Murakami et al. 2004; Tsuchiya et al. 2004). Some high pressure studies (Wang et al. 1991; Shim et al. 2001) suggested the possibility for the existence of a perovskite phase with different symmetry intervening between the *Pbnm* perovskite and the post-perovskite phases. In particular, Wang et al. (1991) reported from X-ray diffraction experiments up to 1253 K at a constant pressure of 7.3 GPa that such a phase transition occurred near 600 K under this pressure. However, the tilt angles at ambient condition of $MgSiO_3$ perovskite calculated using the structural parameters in the published literature (Sugahara et al. 2006) are $\phi_x^- = 11.7°$ and $\phi_z^+ = 11.6°$, much larger than those of $CaGeO_3$ ($\phi_x^- = 7.2°$, $\phi_z^+ = 7.7°$) and $CaTiO_3$ ($\phi_x^- = 8.3°$, $\phi_z^+ = 8.8°$) shown in Figure 10. $MgSiO_3$ should have the phase transition temperature T_c much higher than those of the other two perovskites because the larger tilting yields the higher T_c when $M_A/M_B < 1$ as mentioned above. The increase in T_c is further promoted by the increase in pressure. If the same sequence of the high-temperature phase transitions as $CaTiO_3$ perovskite also appears in $MgSiO_3$ perovskite under high pressures, thus, T_c should become further much higher than those (1512 K for the *Pbnm* to *I4/mcm* transition and 1635

K for the *I4/mcm* to *Pm*$\bar{3}$*m* transition; Yashima and Ali 2009) observed in $CaTiO_3$ perovskite at ambient pressure. The phase transition near 600 K at 7.3 GPa suggested in $MgSiO_3$ perovskite (Wang et al. 1991) is therefore unlikely.

Finally, we emphasize the Earth-scientific significance for the experimental determination of the Debye temperatures from MSDs and for its application to the Earth's interior materials and their related materials. The Debye temperature is generally evaluated from macroscopic properties such as heat capacity and volumetric thermal expansion; these approaches only provide the values averaged for the whole constituent atoms in crystals and over all directions. In contrast, the Debye model fitting to temperature dependence of MSDs determined from X-ray diffraction can not only determine the Debye temperatures individually for each constituent atom in crystals but also provide their anisotropies. The determination of anisotropies in the Debye temperatures of each atom enables the quantitative estimation of anisotropies in the magnitudes of interatomic interactions as shown in the present discussion on OPP. Moreover, the Debye model fitting to temperature dependence of MSDs is a good approach to detect the static disorders of atoms and evaluate the directions and quantities of atomic displacements due to the static disorders, as shown in our previous study on pyrope garnet (Nakatsuka et al. 2011). Consequently, we can separately discuss the dynamic nature and the static nature of the atomic disorders in crystals including the static disorder. Since the static disorders of atoms influence entropy and hence free energy, the separation of dynamic disorder components and static disorder components from MSDs is important to discuss energetic structural stabilities of crystals from microscopic viewpoints. Application of the Debye model fitting to temperature dependence of MSDs to various Earth's interior materials and their related materials can thus provide significant insights into their structural stabilities, being promising for further understanding of the mechanisms of phase transformations occurring in the Earth's interior.

ACKNOWLEDGMENTS

This work was partly performed under the research project (No. 2010G608) at Photon Factory BL-10A, High Energy Accelerator Research Organization, Tsukuba, Japan. We thank Mr. H. Tsukamoto, Mr. K. Tsutsui and Mr. Y. Ueno of Yamaguchi University for their experimental assistance.

REFERENCES CITED

Ali, R., and Yashima, M. (2005) Space group and crystal structure of the perovskite $CaTiO_3$ from 296 to 1720 K. Journal of Solid State Chemistry, 178, 2867–2872.

Allmann, R. (1975) Relations between bond lengths and bond strengths in oxide structures. Monatshefte für Chemie, 106, 779–793.

Anderson, O.L. (1966) Derivation of Wachtman's equation for the temperature dependence of elastic moduli of oxide compounds. Physical Review, 144, 553–557.

Angel, R.J., Zhao, J., and Ross, N.L. (2005) General rules for predicting phase transitions in perovskites due to octahedral tilting. Physical Review Letters, 95, 025503.

Becker, P.J., and Coppens, P. (1974a) Extinction within the limit of validity of the Darwin transfer equations. I. General formalisms for primary and secondary extinction and their application to spherical crystals. Acta Crystallographica, A30, 129–147.

Becker, P.J., and Coppens, P. (1974b) Extinction within the limit of validity of the Darwin transfer equations. II. Refinement of extinction in spherical crystals of SrF_2 and LiF. Acta Crystallographica, A30, 148–153.

Brown, I.D., and Altermatt, D. (1985) Bond-valence parameters obtained from a systematic analysis of the Inorganic Crystal Structure Database. Acta Crystallographica B41, 244–247.

Campbell, B.J., Stokes, H.T., Tanner, D.E., and Hatch, D.M. (2006) ISODISPLACE: a web-based tool for exploring structural distortions. Journal of Applied Crystallography, 39, 607–614.

Dekura, H., Tsuchiya, T., and Tsuchiya, J. (2013) Ab initio lattice thermal conductivity of $MgSiO_3$ perovskite as found in earth's lower mantle. Physical Review Letters, 110, 025904.

Durben D.J., Wolf, G.H., and McMillan P.F. (1991) Raman scattering study of the high-temperature vibrational properties and stability of $CaGeO_3$ perovskite. Physics and Chemistry of Minerals, 18, 215–223.

Fei, Y. (1995) Thermal expansion. AGU Reference Shelf 2: Mineral Physics and Crystallography — A Handbook of Physical Constants, edited by T. J. Ahrens, p. 29–44, Washington.

Glazer, A.M. (1972) The classification of tilted octahedra in perovskites. Acta Crystallographica, B28, 3384–3392.

Glazer, A.M. (1975) Simple ways of determining perovskite structures. Acta Crystallographica, A31, 756–762.

Guyot, F., Richet, P., Courtial, Ph., and Gillet, Ph. (1993) High-temperature heat capacity and phase transitions of $CaTiO_3$ perovskite. Physics and Chemistry of Minerals, 20, 141–146.

Horiuchi, H., Ito, E., and Weidner, D.J. (1987) Perovskite-type $MgSiO_3$: Single-crystal X-ray diffraction study. American Mineralogist, 72, 357–360.

Kennedy, B.J., Howard, C.J., and Chakoumakos, B.C. (1999) Phase transitions in perovskite at elevated temperatures – A powder neutron diffraction study. Journal of Physics: Condensed Matter, 11, 1479–1488.

Kudoh, Y., Ito, E., and Takeda, H. (1987) Effect of pressure on the crystal structure of perovskite-type $MgSiO_3$. Physics and Chemistry of Minerals, 14, 350–354.

Liu, W., Kung, J., Wang, L., and Li, B. (2008) Thermal equation of state of $CaGeO_3$ perovskite. American Mineralogist, 93, 745–750.

Liu, W., and Li, B. (2007) Compressional and shear-wave velocities of the polycrystalline $CaGeO_3$ perovskite to 10 GPa. Physical Review B, 75, 024107.

Liu, X., and Liebermann, R.C. (1993) X-ray powder diffraction study of $CaTiO_3$ perovskite at high temperatures. Physics and Chemistry of Minerals, 20, 171–175.

Liu, X., Wang, Y., Liebermann, R.C., Maniar, P.D., and Navrotsky, A. (1991) Phase transition in $CaGeO_3$ perovskite: evidence from X-ray powder diffraction, thermal expansion and heat capacity. Physics and Chemistry of Minerals, 18, 224–230.

Madon, M., Guyot, F., Peyronneau, J., and Poirier, J.P. (1989) Electron microscopy of high-pressure phases synthesized from natural olivine in diamond anvil cell. Physics and Chemistry of Minerals, 16, 320–330.

McMillan, P., and Ross, N. (1988) The Raman spectra of several orthorhombic calcium oxide perovskites. Physics and Chemistry of Minerals, 16, 21–28.

Murakami, M., Hirose, K., Kawamura, K., Sata, N., and Ohishi, Y. (2004) Post-perovskite phase transition in $MgSiO_3$. Science, 304, 855–858.

Nakatsuka, A., Shimokawa, M., Nakayama, N., Ohtaka, O., Arima, H., Okube, M., and Yoshiasa, A. (2011) Static disorders of atoms and experimental determination of Debye-temperature in pyrope: Low- and high-temperature single crystal X-ray diffraction study. American Mineralogist, 96, 1593–1605.

Prewitt, C.T., and Sleight, A.W. (1969) Garnet-like structures of high-pressure cadmium germanate and calcium germanate. Science, 163, 386–387.

Ringwood, A.E., and Major, A. (1967) Some high-pressure transformations of geophysical significance.

Earth and Planetary Science Letters, 2, 106–110.

Ross, N.L., and Hazen, R.M. (1989) Single crystal X-ray diffraction study of $MgSiO_3$ perovskite from 77 to 400 K. Physics and Chemistry of Minerals, 16, 415–420.

Sasaki, S. (1987) RADY. A Fortran program for the least –squares refinement of crystal structures. National Laboratory for High Energy Physics, Japan.

Sasaki, S., Prewitt, C.T., and Liebermann, R.C. (1983) The crystal structure of $CaGeO_3$ perovskite and the crystal chemistry of the $GdFeO_3$-type perovskites. American Mineralogist, 68, 1189–1198.

Shim, S.-H., Duffy, T.S., and Shen, G. (2001) Stability and structure of $MgSiO_3$ perovskite to 2300-kilometer depth in earth's mantle. Science, 293, 2437–2440.

Sugahara, M., Yoshiasa, A., Komatsu, Y., Yamanaka, T., Bolfan-Casanova, N., Nakatsuka, A., Sasaki, S., and Tanaka, M. (2006) Reinvestigation of the $MgSiO_3$ perovskite structure at high pressure. American Mineralogist, 91, 533–536.

Susaki, J., Akaogi, M., Akimoto, S., and Shimomura, O. (1985) Garnet-perovskite transformation in $CaGeO_3$: in-situ X-ray measurements using synchrotron radiation. Geophysical Research Letters, 12, 729–732.

Suzuki, I., Okajima, S., and Seya, K. (1979) Thermal expansion of single-crystal manganosite. Journal of Physics of the Earth, 27, 63–69.

Tokonami, M. (1965) Atomic scattering factor for O^{2-}. Acta Crystallographica, 19, 486.

Tsuchiya, T., Tsuchiya, J., Umemoto, K., and Wentzcovitch, R.M. (2004) Phase transition in $MgSiO_3$ perovskite in the earth's lower mantle. Earth and Planetary Science Letters, 224, 241–248.

Wang, D., and Angel, R.J. (2011) Octahedral tilts, symmetry-adapted displacive modes and polyhedral volume ratios in perovskite structures. Acta Crystallographica, B67, 302–314.

Wang, Y., Weidner, D.J., Liebermann, R.C., Liu, X., Ko, J., Vaughan, M.T., Zhao, Y., Yeganeh-Haeri, A., and Pacalo, R.E.G. (1991) Phase transition and thermal expansion of $MgSiO_3$ perovskite. Science, 251, 410–413

Wentzcovitch, R.M., Karki, B.B., Cococcioni, M., and De Gironcoli, S. (2004) Thermoelastic properties of $MgSiO_3$-perovskite: insights on the nature of the earth's lower mantle. Physical Review Letters, 92, 185011–185014.

Willis, B.T.M., and Pryor, A.W. (1975) Thermal vibrations in Crystallography, Cambridge University Press.

Wilson, A.J.C., Ed. (1992) International Tables for Crystallography, vol. C. Kluwer, Dordrecht.

Yashima, M., and Ali, R. (2009) Structural phase transition and octahedral tilting in the calcium titanate. Solid State Ionics, 180, 120–126.

Yoshiasa, A., Sakamoto, D., Okudera, H., Sugahara, M., Ota, K., and Nakatsuka, A. (2005) Electrical conductivities and conduction mechanisms of perovskite-type $Na_{1-x}K_xMgF_3$ (x = 0, 0.1, 1) and $KZnF_3$. Zeitschrift für Anorganische und Allgemeine Chemie, 631, 502–506.

Zhao, J., Ross, N.L., and Angel, R.J. (2004) New view of the high-pressure behaviour of $GdFeO_3$-type perovskites. Acta Crystallographica, B60, 263–271.

Figure captions

Figure 1. Crystal structure of $CaGeO_3$ perovskite: (a) a crystallographic viewing, (b) the projection along $[010]_p$ and (c) the projection along $[001]_p$. Symmetry codes for equivalent atoms are as in Table 3.

Figure 2. Temperature dependence of the unit-cell parameters (a) a_p, b_p, c_p and (b) α_p, β_p, γ_p.

Figure 3. Temperature dependence of the unit-cell volume (V_p) and the volumetric thermal expansion coefficient $\alpha_V(T)$. The fitted curve of the V_p data is based on Equation (1).

Figure 4. Temperature dependence of the ω-scan profile of 200 reflection.

Figure 5. Relationship between $\sqrt{2} \times \sqrt{2} \times 2$ and $2 \times 2 \times 2$ lattices.

Figure 6. Temperature dependence of the ω-scan profiles measured at the positions of 104, 300 and 302 reflections. These correspond to 114, 330 and 332 reflections in the $2 \times 2 \times 2$ lattice, respectively.

Figure 7. Temperature dependence of the unit-cell edge lengths in pseudo-cubic lattice ($\sqrt{2}a_p/2$, $\sqrt{2}b_p/2$ and $c_p/2$).

Figure 8. Temperature dependence of the interatomic distances.

Figure 9. Temperature dependence of the thermal expansion coefficients $\alpha_L(T)$ of unit-cell edge lengths and interatomic distances.

Figure 10. Temperature dependence of (a) the octahedral tilt angles ϕ_x^- and ϕ_z^+ calculated from the symmetry-adapted mode approach (Wang and Angel, 2011) and (b) the Ca positional parameters. Solid and open symbols represent $CaGeO_3$ perovskite (the present study) and $CaTiO_3$ perovskite (Yashima and Ali, 2009), respectively. The sharp decrease in ϕ_x^- of $CaTiO_3$ perovskite is observed at the temperature beyond 1423 K owing to the approach of the phase transition to the *I4/mcm*

tetragonal phase at 1512 K.

Figure 11. Temperature dependence of U_{eq}. Solid curves represent the Debye model fitting.

Figure 12. Temperature dependence of MSD_{hkl} (hkl = 100, 010, 001, 110) in the $[hkl]_p$ directions. In the O2 atom, MSD in the direction of the shortest ellipsoid-axis is plotted as MSD_{110} because the axis is parallel nearly to $[110]_p$ within ±2° over the investigated temperature range. Solid curves represent the Debye model fitting.

Figure 13. Displacement ellipsoids at 298 K projected along $[001]_p$. Atoms are drawn at 80% probability level.

Table 1. Summary of data collection and refinement parameters

T(K)	98	123	173	223	273	298
Cell setting	orthorhombic	orthorhombic	orthorhombic	orthorhombic	orthorhombic	orthorhombic
Space group	*Pbnm*	*Pbnm*	*Pbnm*	*Pbnm*	*Pbnm*	*Pbnm*
a (Å)	5.2539(3)	5.2544(4)	5.2564(3)	5.2585(3)	5.2609(2)	5.2631(3)
b (Å)	5.2672(4)	5.2680(5)	5.2687(4)	5.2694(4)	5.2705(3)	5.2709(3)
c (Å)	7.4354(5)	7.4376(6)	7.4402(5)	7.4433(5)	7.4466(3)	7.4485(4)
V(Å^3)	205.76(2)	205.88(3)	206.06(2)	206.25(2)	206.49(2)	206.64(2)
$2\theta_{max}$ (°)	100	100	100	100	100	100
No. of measured reflections	2446	2446	2448	2450	2450	2454
No. of independent reflections						
No. of observed reflections [$F_o > 3\sigma(F_o)$]						
R_{int}	0.0101	0.0097	0.0099	0.0092	0.0094	0.0093
No. of reflections using refinements	844	833	827	821	799	798
No. of parameters	29	29	29	29	29	29
R	0.0152	0.0144	0.0151	0.0156	0.0159	0.0152
wR	0.0141	0.0125	0.0143	0.0145	0.0148	0.0143

T(K)	323	373	423	473	523	573
Cell setting	orthorhombic	orthorhombic	orthorhombic	orthorhombic	orthorhombic	orthorhombic
Space group	*Pbnm*	*Pbnm*	*Pbnm*	*Pbnm*	*Pbnm*	*Pbnm*
a (Å)	5.2644(2)	5.2673(3)	5.2697(3)	5.2722(4)	5.2748(4)	5.2779(4)
b (Å)	5.2719(2)	5.2733(3)	5.2750(4)	5.2768(4)	5.2782(5)	5.2801(5)
c (Å)	7.4507(3)	7.4548(4)	7.4581(4)	7.4615(5)	7.4646(6)	7.4689(6)
V(Å^3)	206.78(1)	207.07(2)	207.33(2)	207.60(2)	207.83(3)	208.15(3)
$2\theta_{max}$ (°)	100	100	100	100	100	100
No. of measured reflections	2455	2458	2458	2459	2474	2482
No. of independent reflections						
No. of observed reflections [$F_o > 3\sigma(F_o)$]						
R_{int}	0.0102	0.0096	0.0096	0.0123	0.0116	0.0116
No. of reflections using refinements	788	769	747	745	742	727
No. of parameters	29	29	29	29	29	29
R	0.0154	0.0161	0.0144	0.0212	0.0142	0.0148
wR	0.0143	0.0143	0.0122	0.0158	0.0127	0.0125

T(K)	623	673	723	773	823	873
Cell setting	orthorhombic	orthorhombic	orthorhombic	orthorhombic	orthorhombic	orthorhombic
Space group	*Pbnm*	*Pbnm*	*Pbnm*	*Pbnm*	*Pbnm*	*Pbnm*
a (Å)	5.2815(3)	5.2845(4)	5.2880(4)	5.2919(4)	5.2956(4)	5.2992(3)
b (Å)	5.2825(3)	5.2847(4)	5.2875(4)	5.2904(4)	5.2928(4)	5.2958(4)
c (Å)	7.4741(4)	7.4782(5)	7.4829(5)	7.4884(5)	7.4929(5)	7.4980(4)
V(Å^3)	208.54(2)	208.85(2)	209.23(3)	209.66(3)	210.03(3)	210.43(2)
$2\theta_{max}$ (°)	100	100	100	100	100	100
No. of measured reflections	2482	2486	2506	2506	2508	2522
No. of independent reflections						
No. of observed reflections [$F_o > 3\sigma(F_o)$]						
R_{int}	0.0130	0.0113	0.0125	0.0130	0.0138	0.0203
No. of reflections using refinements	714	687	689	677	659	653
No. of parameters	29	29	29	29	29	29
R	0.0147	0.0157	0.0156	0.0154	0.0147	0.0229
wR	0.0118	0.0126	0.0126	0.0128	0.0117	0.0184

Table 2. Refined positional parameters and equivalent isotropic displacement parameters U_{eq} (Å^2)

	T (K)	98	123	173	223	273	298
Ca (4*c*)	x	−0.00571(9)	−0.00565(9)	−0.00553(10)	−0.00533(10)	−0.00517(11)	−0.00509(11)
	y	0.03055(5)	0.03033(5)	0.02979(5)	0.02920(6)	0.02850(6)	0.02819(6)
	z	0.25	0.25	0.25	0.25	0.25	0.25
	U_{eq}	0.00255(5)	0.00285(5)	0.00345(5)	0.00425(5)	0.00518(6)	0.00554(5)
Ge (4*b*)	x	0	0	0	0	0	0
	y	0.5	0.5	0.5	0.5	0.5	0.5
	z	0	0	0	0	0	0
	U_{eq}	0.00095(3)	0.00112(3)	0.00134(3)	0.00169(4)	0.00215(4)	0.00226(3)
O1 (4*c*)	x	0.0639(3)	0.0635(2)	0.0627(3)	0.0627(3)	0.0618(3)	0.0616(3)
	y	0.4898(3)	0.4898(2)	0.4901(3)	0.4902(3)	0.4904(3)	0.4904(3)
	z	0.25	0.25	0.25	0.25	0.25	0.25
	U_{eq}	0.0036(2)	0.0039(2)	0.0043(2)	0.0049(2)	0.0056(3)	0.0059(2)
O2 (8*d*)	x	0.7151(2)	0.7150(2)	0.7152(2)	0.7155(2)	0.7155(2)	0.7158(2)
	y	0.2841(2)	0.2839(2)	0.2837(2)	0.2838(2)	0.2836(2)	0.2835(2)
	z	0.0326(1)	0.0327(1)	0.0326(1)	0.0324(1)	0.0321(1)	0.0322(1)
	U_{eq}	0.0030(2)	0.0031(2)	0.0035(2)	0.0041(2)	0.0050(2)	0.0052(2)
	T (K)	323	373	423	473	523	573
Ca (4*c*)	x	−0.00494(11)	−0.00484(11)	−0.00463(10)	−0.00448(14)	−0.00448(11)	−0.00431(12)
	y	0.02786(6)	0.02710(6)	0.02641(5)	0.02584(7)	0.02534(6)	0.02465(6)
	z	0.25	0.25	0.25	0.25	0.25	0.25
	U_{eq}	0.00601(6)	0.00710(6)	0.00794(5)	0.00884(8)	0.00920(6)	0.01003(6)
Ge (4*b*)	x	0	0	0	0	0	0
	y	0.5	0.5	0.5	0.5	0.5	0.5
	z	0	0	0	0	0	0
	U_{eq}	0.00254(4)	0.00313(4)	0.00350(3)	0.00392(4)	0.00395(3)	0.00433(3)
O1 (4*c*)	x	0.0612(3)	0.0606(3)	0.0596(2)	0.0598(3)	0.0597(3)	0.0594(3)
	y	0.4908(3)	0.4908(3)	0.4911(3)	0.4913(4)	0.4913(3)	0.4914(3)
	z	0.25	0.25	0.25	0.25	0.25	0.25
	U_{eq}	0.0062(2)	0.0072(3)	0.0080(2)	0.0087(3)	0.0091(3)	0.0097(3)
O2 (8*d*)	x	0.7159(2)	0.7163(2)	0.7163(2)	0.7163(2)	0.7168(2)	0.7171(2)
	y	0.2833(2)	0.2830(2)	0.2829(2)	0.2827(2)	0.2826(2)	0.2822(2)
	z	0.0320(1)	0.0319(1)	0.0315(1)	0.0313(2)	0.0311(1)	0.0310(1)
	U_{eq}	0.0057(2)	0.0066(2)	0.0073(2)	0.0080(2)	0.0083(2)	0.0092(2)
	T (K)	623	673	723	773	823	873
Ca (4*c*)	x	−0.00413(11)	−0.00405(13)	−0.00381(13)	−0.00374(15)	−0.00350(13)	−0.00337(22)
	y	0.02395(6)	0.02307(7)	0.02234(7)	0.02152(8)	0.02085(8)	0.02002(13)
	z	0.25	0.25	0.25	0.25	0.25	0.25
	U_{eq}	0.01109(6)	0.01223(6)	0.01330(8)	0.01439(8)	0.01524(8)	0.01646(11)
Ge (4*b*)	x	0	0	0	0	0	0
	y	0.5	0.5	0.5	0.5	0.5	0.5
	z	0	0	0	0	0	0
	U_{eq}	0.00482(3)	0.00532(4)	0.00586(4)	0.00634(4)	0.00666(3)	0.00738(5)
O1 (4*c*)	x	0.0589(3)	0.0575(3)	0.0574(3)	0.0568(3)	0.0563(3)	0.0556(4)
	y	0.4916(3)	0.4918(4)	0.4920(4)	0.4921(4)	0.4925(4)	0.4926(6)
	z	0.25	0.25	0.25	0.25	0.25	0.25
	U_{eq}	0.0107(3)	0.0118(3)	0.0129(3)	0.0141(3)	0.0145(3)	0.0154(5)
O2 (8*d*)	x	0.7174(2)	0.7176(2)	0.7179(2)	0.7184(2)	0.7186(2)	0.7189(3)
	y	0.2819(2)	0.2817(2)	0.2814(2)	0.2808(2)	0.2807(2)	0.2802(3)
	z	0.0306(1)	0.0303(1)	0.0300(1)	0.0298(1)	0.0294(1)	0.0291(2)
	U_{eq}	0.0102(2)	0.0111(2)	0.0122(2)	0.0133(2)	0.0141(2)	0.0153(4)

Table 3. Temperature-dependent thermal expansion coefficients $\alpha_L(T)$ (K^{-1}) of unit-cell edge lengths and interatomic distances expressed by the polynomial approximation and their mean thermal expansion coefficients $\langle\alpha_L\rangle$ (K^{-1})

	$\alpha_L(T) = \varepsilon_0 + \varepsilon_1 T + \varepsilon_2 T^{-2}$ ($\varepsilon_2 \le 0$)			$\langle\alpha_L\rangle \times 10^5$
	$\varepsilon_0 \times 10^5$	$\varepsilon_1 \times 10^8$	$\varepsilon_2 \times 10^3$	
	Unit-cell edge lengths			
a_p	0.7547	0.7478	−0.2982	1.13(1)
b_p	0.1140	1.1951	−0.2829	0.71(2)
c_p	0.7029	0.7519	−0.2859	1.08(1)
	Non-bonding Ca···O			
Ca···O1^{i}	−2.8606	0.1958	0	−2.75(3)
Ca···O1^{ii}	−0.7143	0.7297	0	−0.36(5)
Ca···O2^{iii} (= Ca···O2^{iv})	−1.3913	−1.6781	−1.0745	−2.19(4)
	Ca–O bonds			
Ca–O1^{v}	1.9162	1.0322	−0.7695	2.42(6)
Ca–O1	2.8784	2.1918	−2.6707	3.96(6)
Ca–O2^{vi} (= Ca–O2^{v})	0.3767	2.9298	−1.4931	1.79(6)
Ca–O2^{vii} (= Ca–O2^{viii})	2.0241	1.0590	−0.8309	2.54(3)
Ca–O2^{ix} (= Ca–O2^{x})	0.9943	1.2121	−0.5723	1.58(4)
<Ca–O>	1.6406	1.6767	−1.2430	2.46(4)
	Ge–O bonds			
Ge–O1 (= Ge–O1^{xi})	0.1520	0.8782	−0.1440	0.57(2)
Ge–O2^{ix} (= Ge–O2^{xii})	0.3326	0.1859	−0.0237	0.42(2)
Ge–O2^{vii} (= Ge–O2^{xiii})	0.0643	0.7506	−0.0900	0.43(3)
<Ge–O>	0.1828	0.6051	−0.0829	0.47(1)

Symmetry codes for equivalent atoms:

(i) $x, y-1, z$; (ii) $-x-\frac{1}{2}, y-\frac{1}{2}, z$; (iii) $-x+1, -y, z+\frac{1}{2}$; (iv) $-x+1, -y, -z$; (v) $-x+\frac{1}{2}, y-\frac{1}{2}, z$; (vi) $-x+\frac{1}{2}, y-\frac{1}{2}, -z+\frac{1}{2}$; (vii) $x-1, y, z$; (viii) $x-1, y, -z+\frac{1}{2}$; (ix) $x-\frac{1}{2}, -y+\frac{1}{2}, -z$; (x) $x-\frac{1}{2}, -y+\frac{1}{2}, z+\frac{1}{2}$; (xi) $-x, -y+1, -z$; (xii) $-x+\frac{1}{2}, y+\frac{1}{2}, z$; (xiii) $-x+1, -y+1, -z$.

Table 4. Interatomic distances (Å) and bond valence sums (BVS) at 298 K

	Distances		*Bond valences †C.N. (Ca) 12	 †C.N. (Ca) 8
Ca				
Ca···O1^{i}	2.8562(16)		0.0961	
Ca···O1^{ii}	2.9358(15)		0.0792	
Ca···O2^{iii} (= Ca···O2^{iv})	3.0719(10)		0.0568 × 2	
Ca–O1^{v}	2.3426(15)		0.3365	0.3365
Ca–O1	2.4616(16)		0.2517	0.2517
Ca–O2^{vi} (= Ca–O2^{v})	2.3504(10)		0.3301 × 2	0.3301× 2
Ca–O2^{vii} (= Ca–O2^{viii})	2.5692(10)		0.1936 × 2	0.1936× 2
Ca–O2^{ix} (= Ca–O2^{x})	2.5991(10)		0.1800 × 2	0.1800× 2
		BVS	2.28	2.00
Ge				
Ge–O1 (= Ge–O1^{xi})	1.8908(3)		0.6798 × 2	0.6798 × 2
Ge–O2^{ix} (= Ge–O2^{xii})	1.8921(10)		0.6774 × 2	0.6774 × 2
Ge–O2^{vii} (= Ge–O2^{xiii})	1.8968(10)		0.6689 × 2	0.6689 × 2
		BVS	4.05	4.05
O1				
Ca^{xiv}···O1	2.8562(16)		0.0961	
Ca^{xv}···O1	2.9358(15)		0.0792	
Ca^{xii}–O1	2.3426(15)		0.3365	0.3365
Ca–O1	2.4616(16)		0.2517	0.2517
Ge–O1 (= Ge^{xvi}–O1)	1.8908(3)		0.6798 × 2	0.6798 × 2
		BVS	2.12	1.95
O2				
Ca^{iv}···O2	3.0719(10)		0.0568	
Ca^{xii}–O2	2.3504(10)		0.3301	0.3301
Ca^{xvii}–O2	2.5692(10)		0.1936	0.1936
Ca^{xviii}–O2	2.5991(10)		0.1800	0.1800
Ge^{v}–O2	1.8921(10)		0.6774	0.6774
Ge^{xiii}–O2	1.8968(10)		0.6689	0.6689
		BVS	2.11	2.05

Symmetry codes for equivalent atoms:

(xiv) $x, y+1, z$; (xv) $-x-\frac{1}{2}, y+\frac{1}{2}, z$; (xvi) $x, y, -z+\frac{1}{2}$; (xvii) $x+1, y, z$; (xviii) $x+\frac{1}{2}, -y+\frac{1}{2}, -z$. The symmetry codes (i)–(xiii) are as in Table 3.

* The bond valence parameters are taken from Allmann (1975) for Ca; from Brown and Altermatt (1985) for Ge.

† C.N.: coordination number

Table 5. Debye temperatures (K) determined from the Debye model fitting

	Ca	Ge	O1	O2
$\Theta_{D_{eq}}$	448(2)	505(3)	728(2)	750(5)
$\Theta_{D_{100}}$	467(3)	521(6)	719(4)	820(9)
$\Theta_{D_{010}}$	436(2)	517(6)	597(3)	831(6)
$\Theta_{D_{001}}$	442(2)	480(3)	1041(13)	646(4)
$\Theta_{D_{110}}$	—	—	—	1149(23)

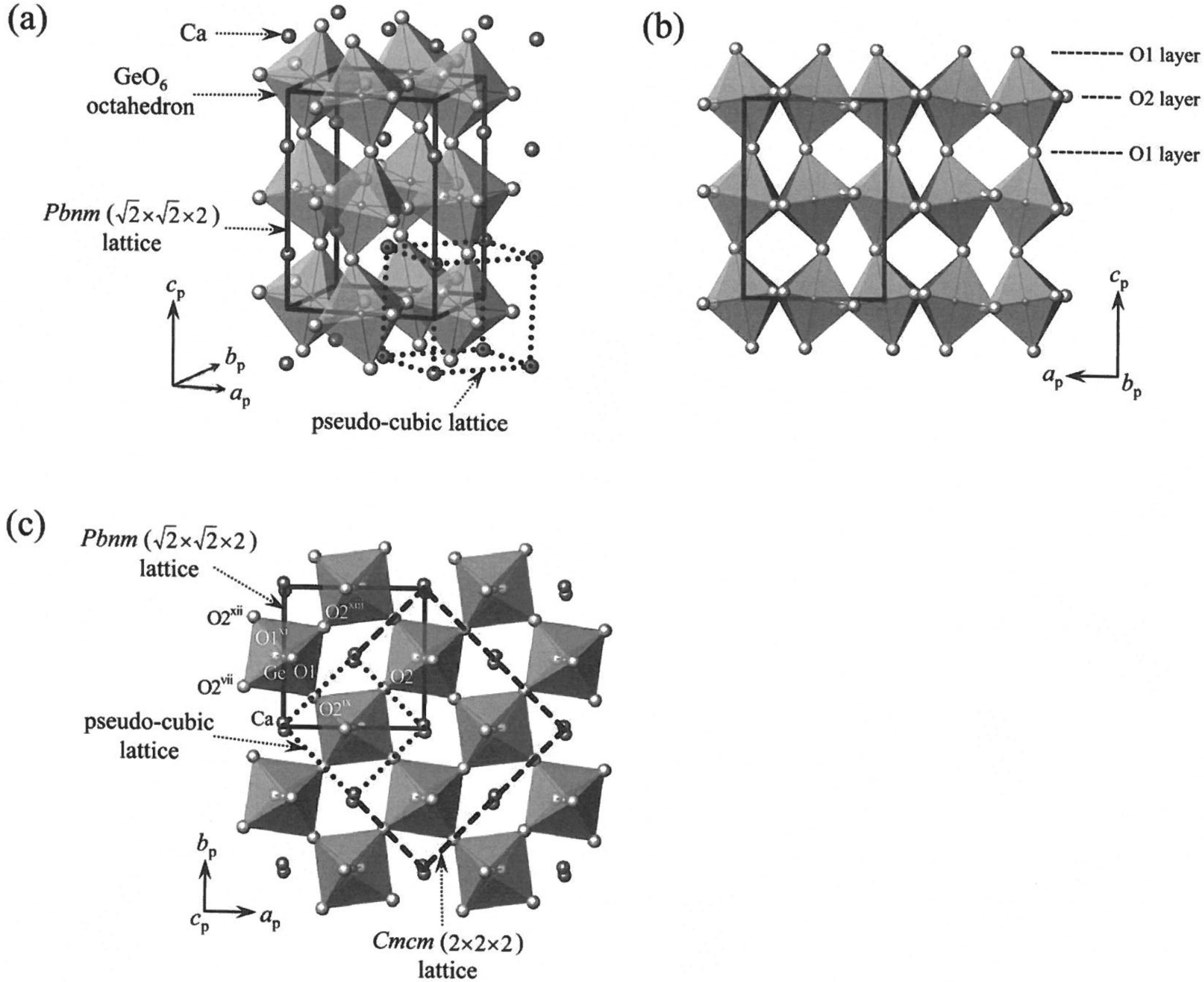
(a)
Ca
GeO6 octahedron
Pbnm (√2×√2×2) lattice
pseudo-cubic lattice
cp
bp
ap
(b)
O1 layer
O2 layer
O1 layer
cp
ap
bp
(c)
Pbnm (√2×√2×2) lattice
O2xii
O1xi
O2xiii
Ge
O1
O2
O2vii
O2ix
Ca
pseudo-cubic lattice
Cmcm (2×2×2) lattice
bp
cp
ap

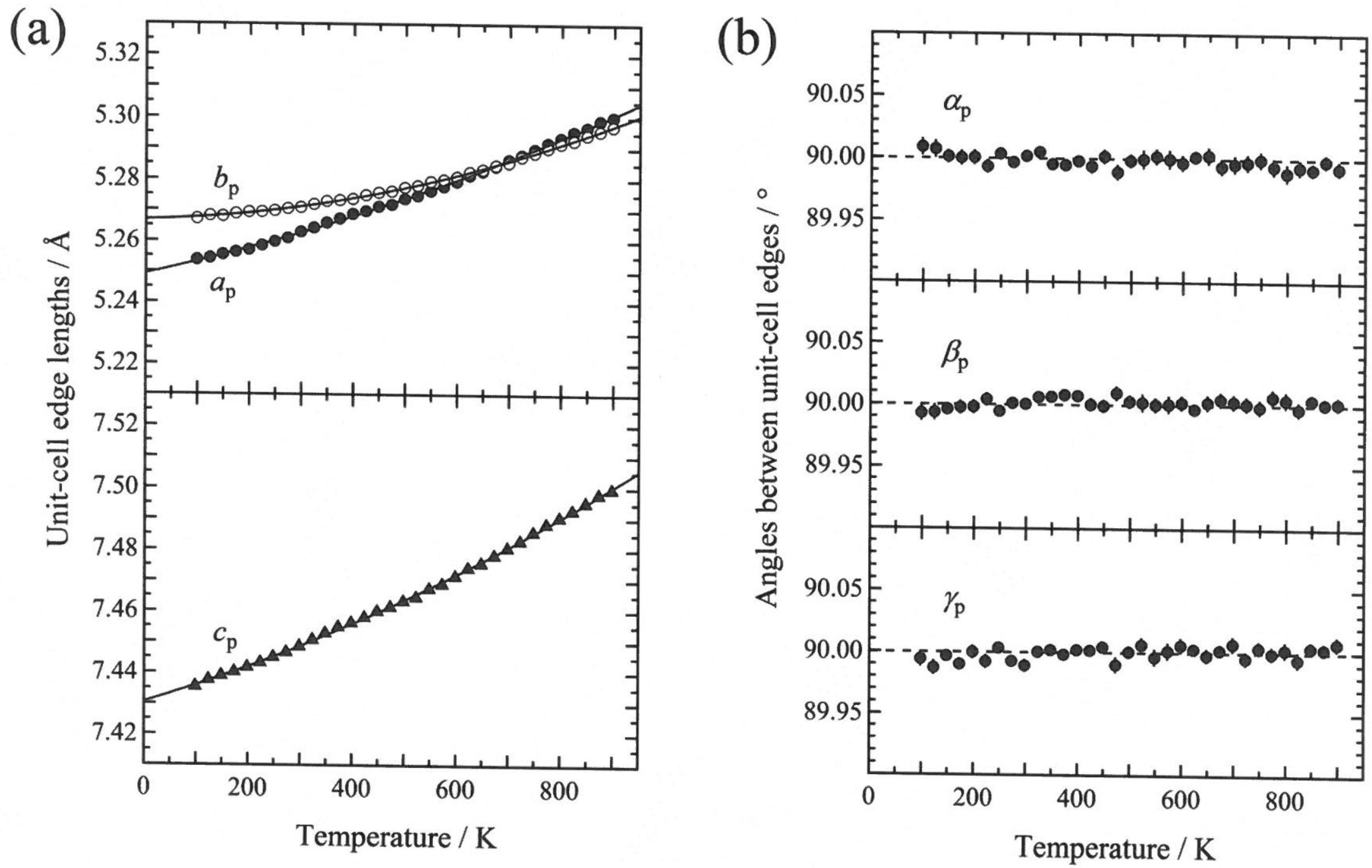
(a)
Unit-cell edge lengths / Å
5.32
5.30
5.28
5.26
5.24
5.22
7.52
7.50
7.48
7.46
7.44
7.42
b_p
a_p
c_p
0
200
400
600
800
Temperature / K
(b)
Angles between unit-cell edges / °
90.05
90.00
89.95
α_p
β_p
γ_p
Temperature / K

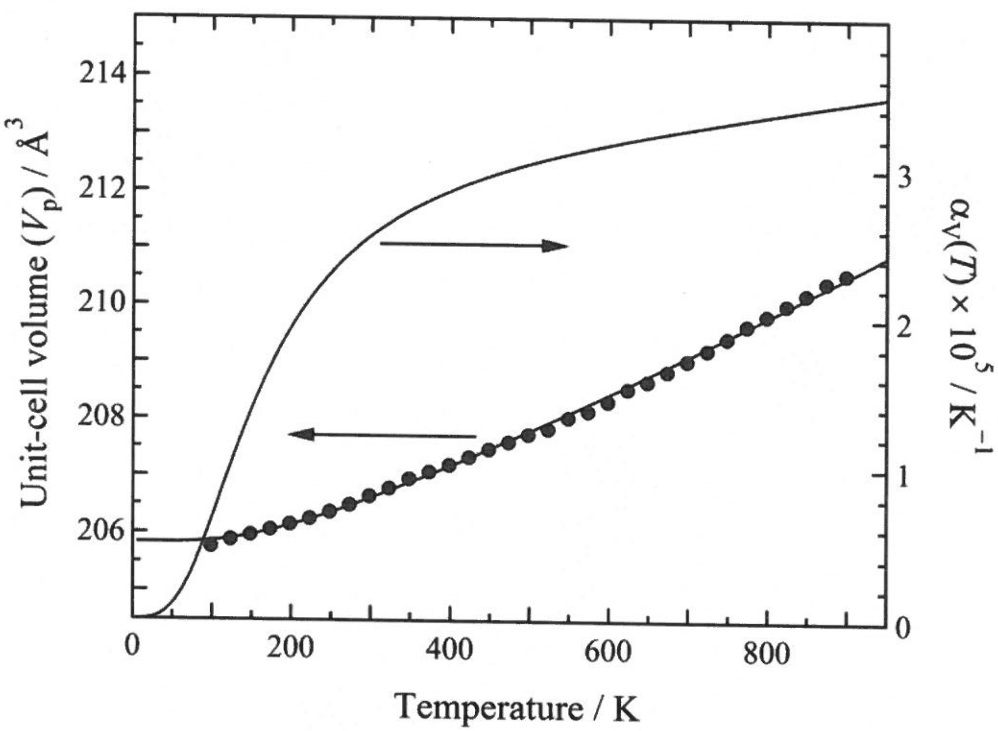

Unit-cell volume (V_p) / Å^3
214
212
210
208
206
0
200
400
600
800
Temperature / K
$\alpha_V(T) \times 10^5$ / K^{-1}
3
2
1
0

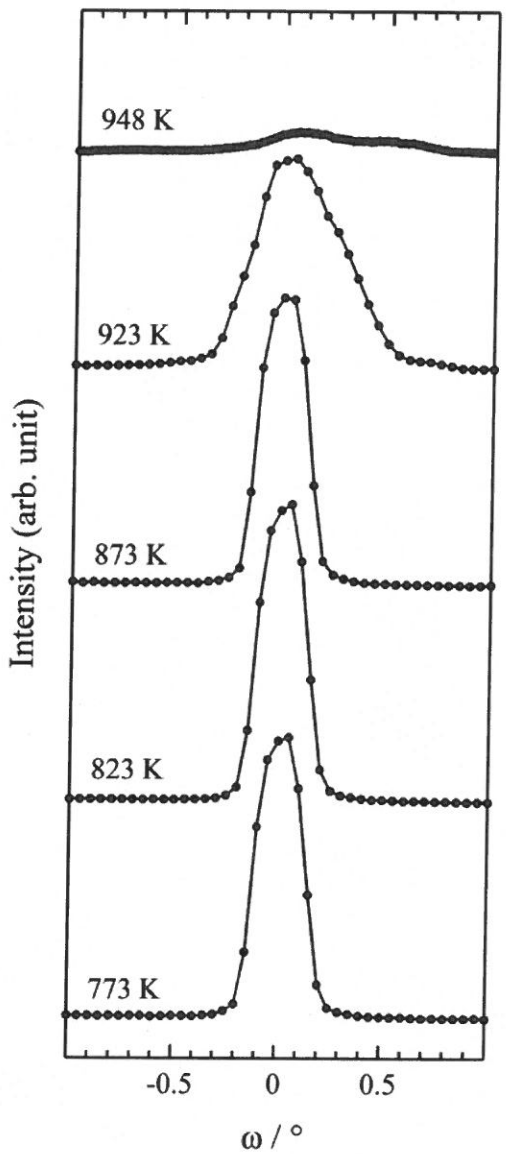
948 K
923 K
873 K
823 K
773 K
Intensity (arb. unit)
-0.5
0
0.5
ω / °

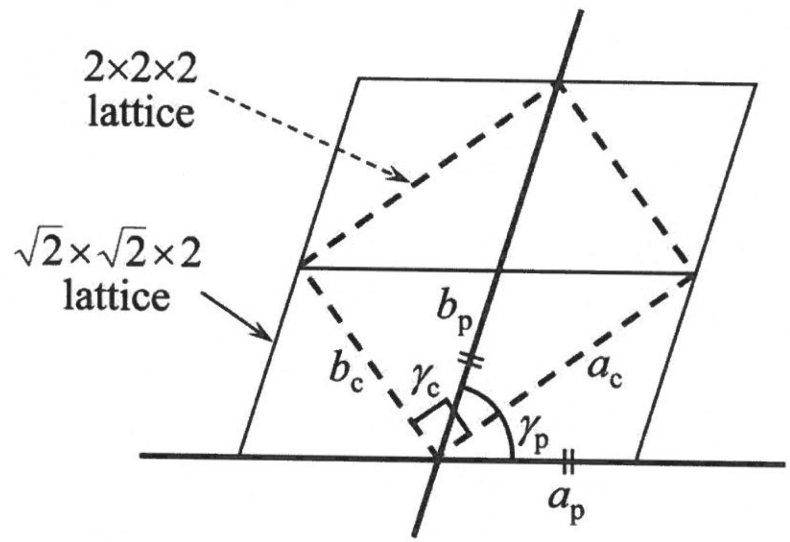
2×2×2
lattice
√2×√2×2
lattice
b_p
b_c
γ_c
a_c
γ_p
a_p

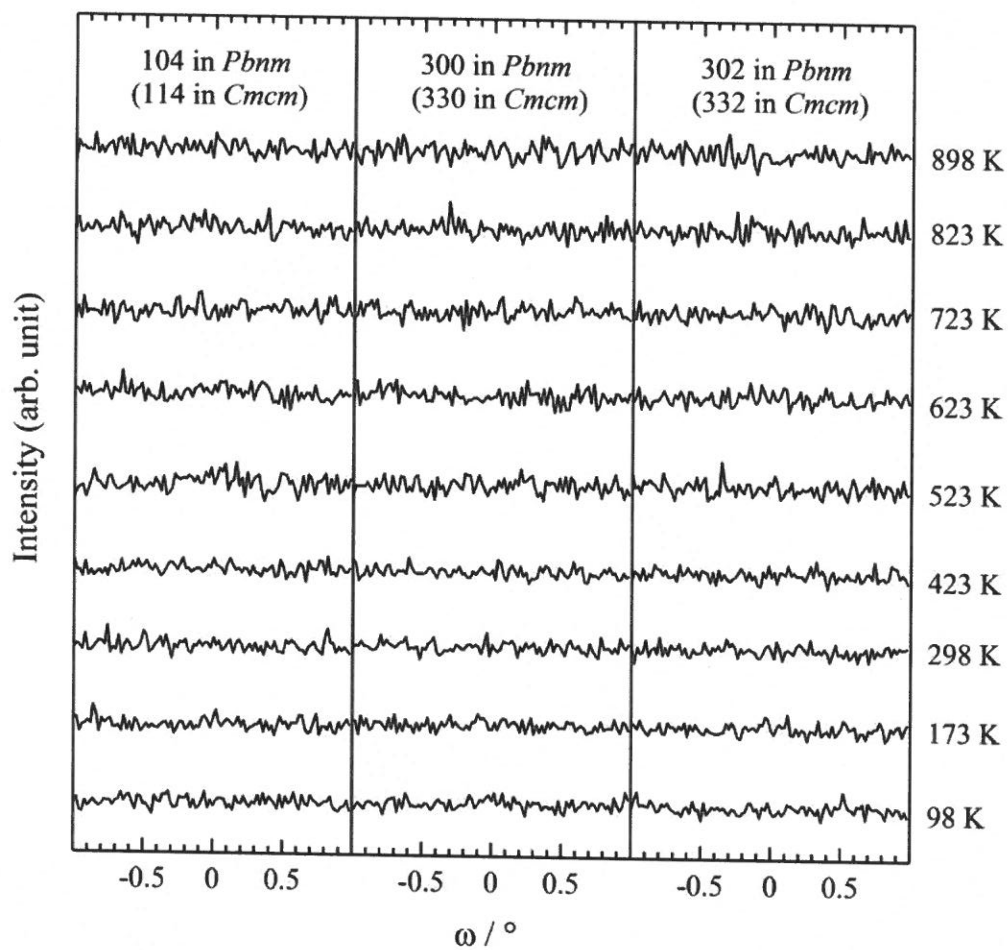

104 in Pbnm
(114 in Cmcm)
300 in Pbnm
(330 in Cmcm)
302 in Pbnm
(332 in Cmcm)
898 K
823 K
723 K
623 K
523 K
423 K
298 K
173 K
98 K
Intensity (arb. unit)
-0.5
0
0.5
ω / °

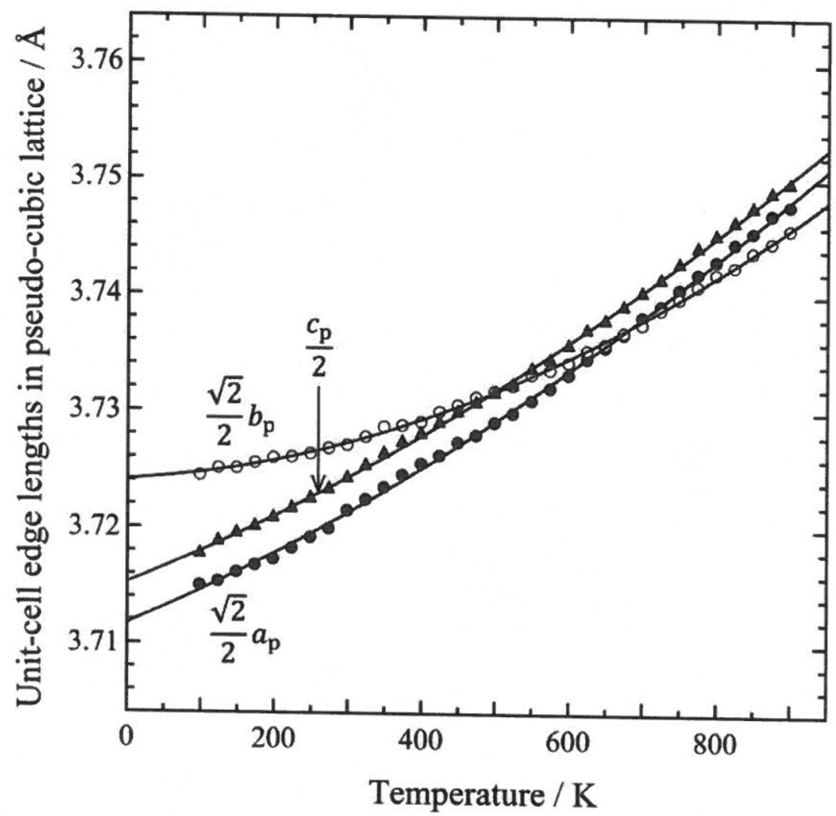
Unit-cell edge lengths in pseudo-cubic lattice / Å
3.76
3.75
3.74
3.73
3.72
3.71
0
200
400
600
800
Temperature / K
$\frac{c_p}{2}$
$\frac{\sqrt{2}}{2} b_p$
$\frac{\sqrt{2}}{2} a_p$

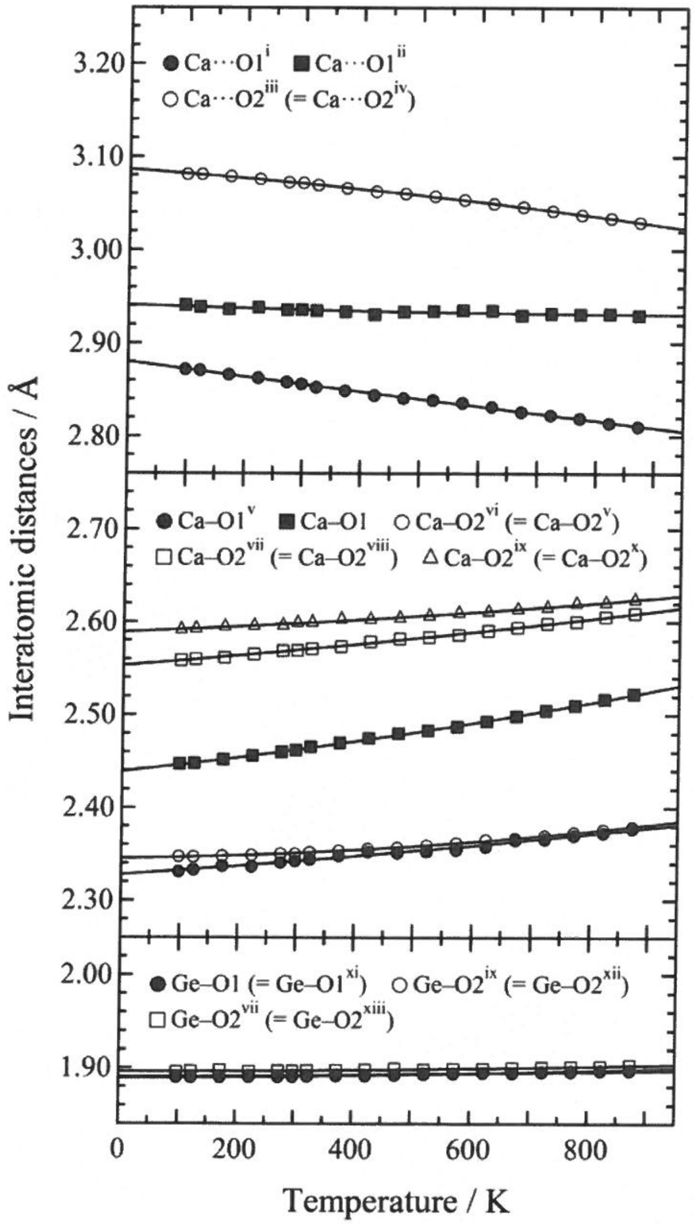

Ca···O1^i ■ Ca···O1^ii
○ Ca···O2^iii (= Ca···O2^iv)
Ca–O1^v ■ Ca–O1 ○ Ca–O2^vi (= Ca–O2^v)
□ Ca–O2^vii (= Ca–O2^viii) △ Ca–O2^ix (= Ca–O2^x)
Ge–O1 (= Ge–O1^xi) ○ Ge–O2^ix (= Ge–O2^xii)
□ Ge–O2^vii (= Ge–O2^xiii)
3.20
3.10
3.00
2.90
2.80
2.70
2.60
2.50
2.40
2.30
2.00
1.90
0
200
400
600
800
Interatomic distances / Å
Temperature / K

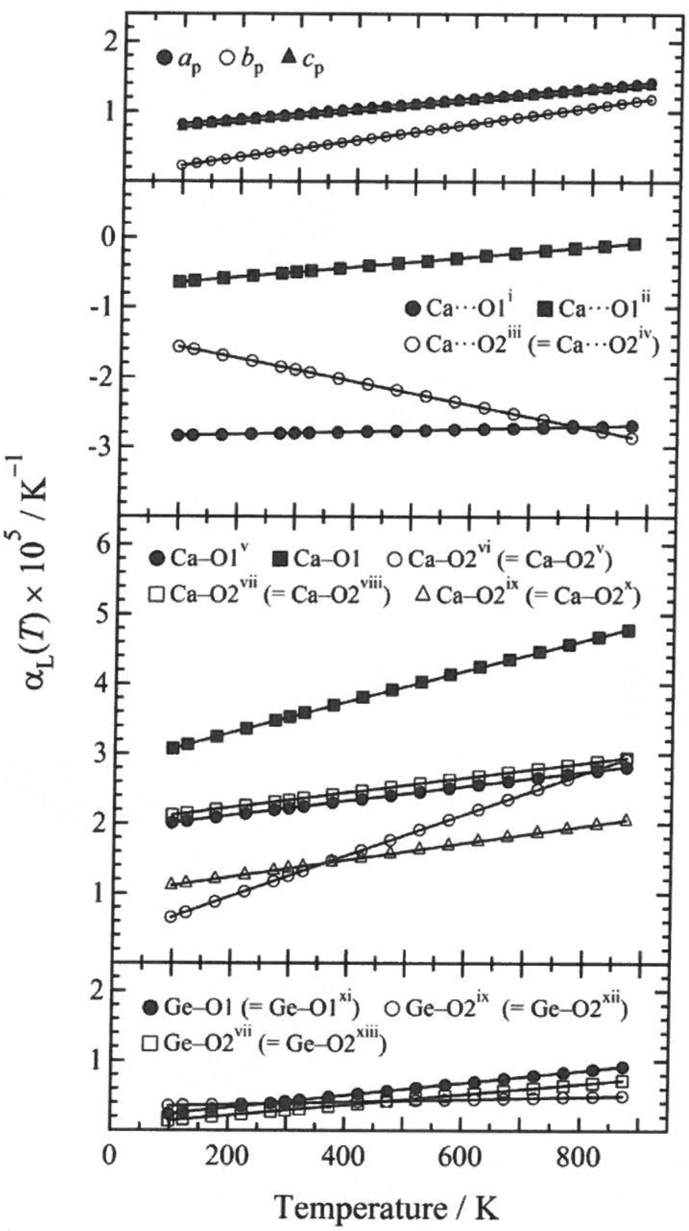

a_p b_p c_p
Ca···O1^i Ca···O1^ii
Ca···O2^iii (= Ca···O2^iv)
Ca–O1^v Ca–O1 Ca–O2^vi (= Ca–O2^v)
Ca–O2^vii (= Ca–O2^viii) Ca–O2^ix (= Ca–O2^x)
Ge–O1 (= Ge–O1^xi) Ge–O2^ix (= Ge–O2^xii)
Ge–O2^vii (= Ge–O2^xiii)
$\alpha_L(T) \times 10^5$ / K^{-1}
Temperature / K
0
200
400
600
800

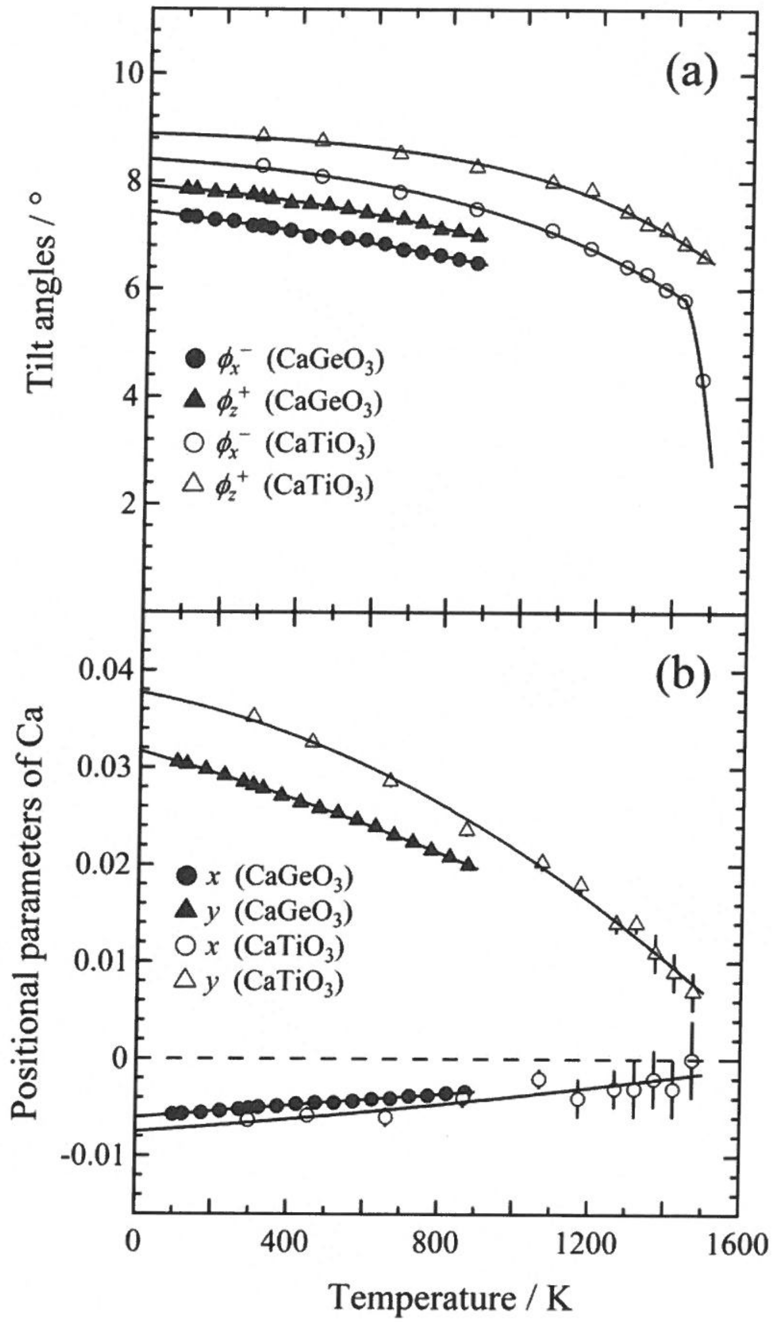

(a)
Tilt angles / °
10
8
6
4
2
ϕ_x^- (CaGeO$_3$)
ϕ_z^+ (CaGeO$_3$)
ϕ_x^- (CaTiO$_3$)
ϕ_z^+ (CaTiO$_3$)
(b)
Positional parameters of Ca
0.04
0.03
0.02
0.01
0
-0.01
x (CaGeO$_3$)
y (CaGeO$_3$)
x (CaTiO$_3$)
y (CaTiO$_3$)
0
400
800
1200
1600
Temperature / K

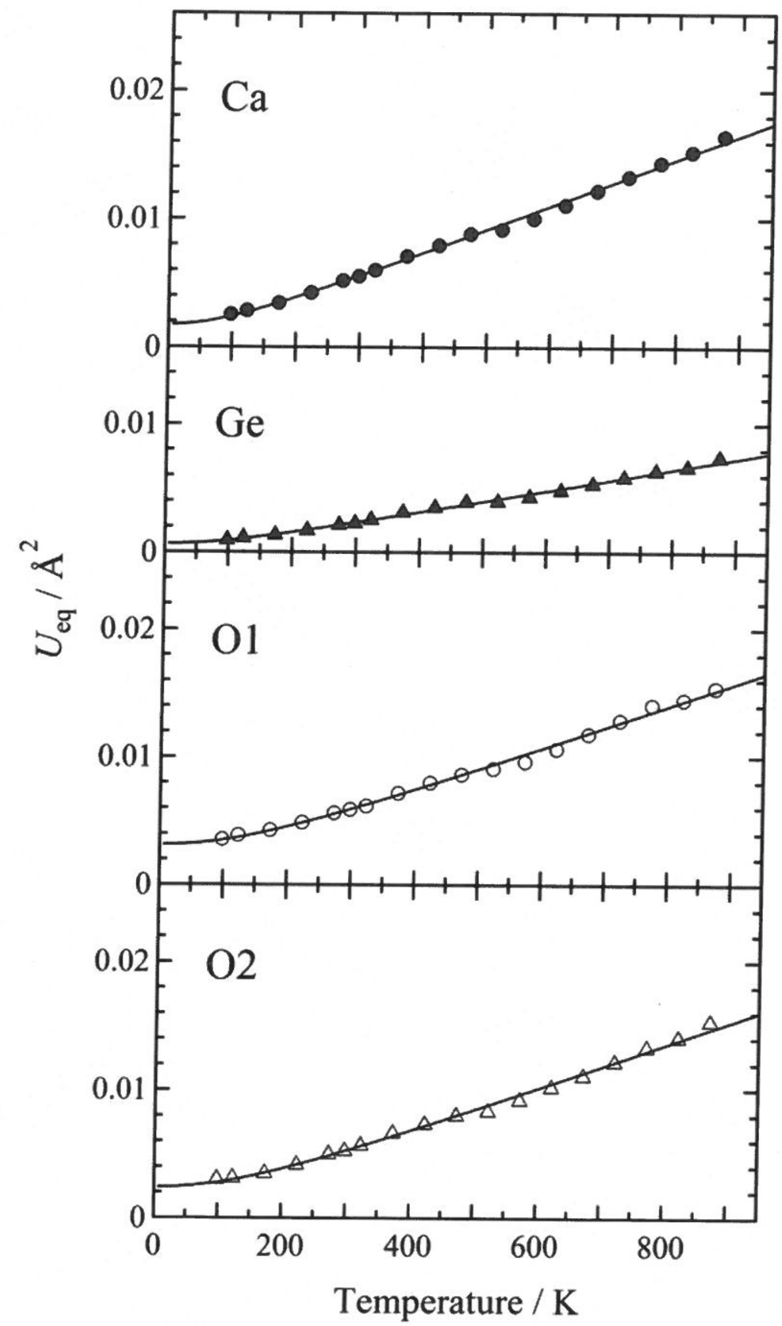

Ca
Ge
O1
O2
0.02
0.01
0
U_{eq} / Å^2
0
200
400
600
800
Temperature / K

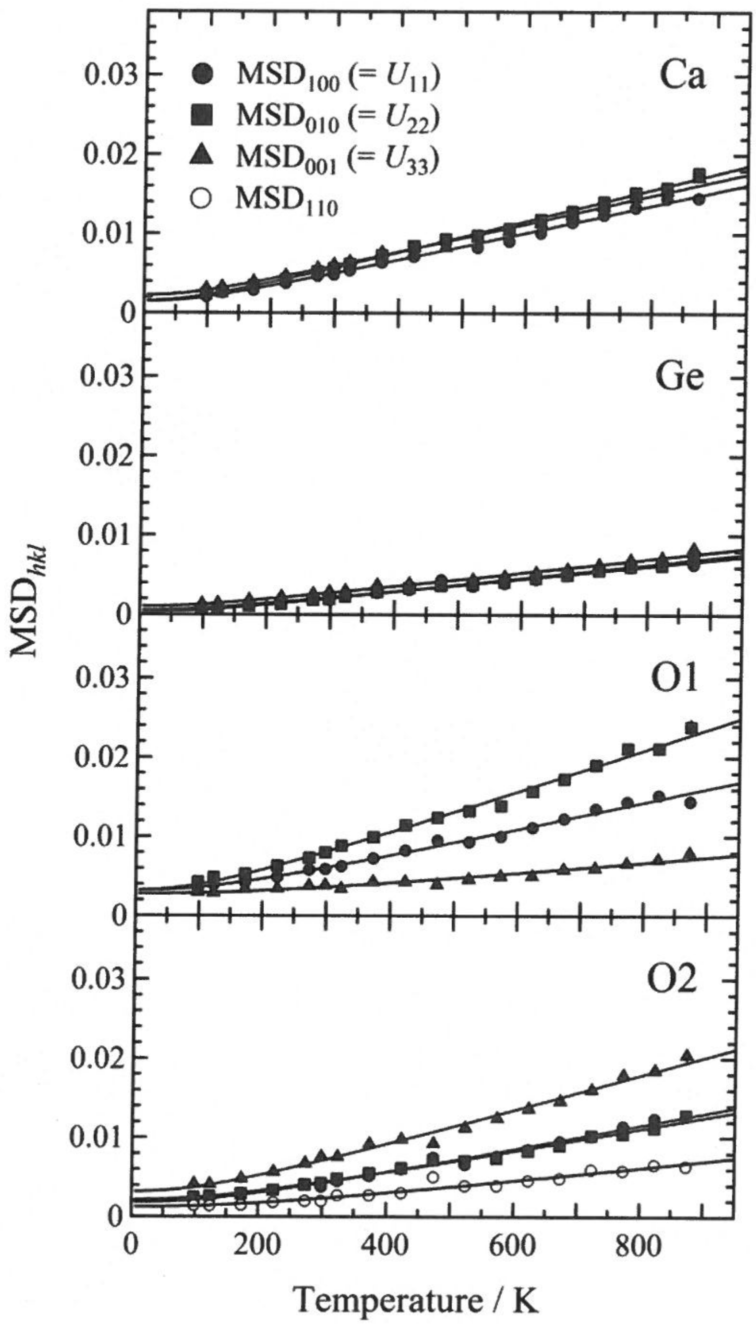

MSD$_{100}$ (= U_{11})
MSD$_{010}$ (= U_{22})
MSD$_{001}$ (= U_{33})
MSD$_{110}$
Ca
Ge
O1
O2
0.03
0.02
0.01
0
MSD$_{hkl}$
0
200
400
600
800
Temperature / K

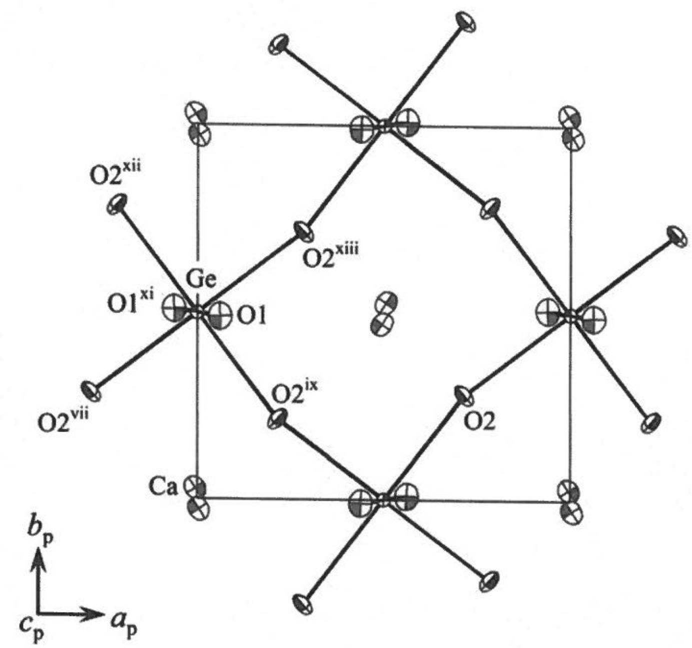
O2^xii
Ge
O1^xi
O1
O2^xiii
O2^ix
O2
O2^vii
Ca
b_p
c_p
a_p